Investigation into nanoindentation-induced 'pop-in' phenomena under the monitoring of acoustic emission

by

Xiaoguang Ma

Submitted in partial satisfaction
of the requirements for the degree of
Master of Science in Mechanical Engineering

Computer Mechanics Laboratory
Department of Mechanical Engineering
University of California at Berkeley 94720

ABSTRACT

The damage mechanisms of 'pop-in' (displacement excursion observed at constant load during indentation) for both bulk crystalline materials and film-substrate systems were investigated by performing nanoindentation tests using cube corner tips with nominal radii of curvature of 116 and 685 nm under the *in-situ* monitoring of acoustic emission. Different types of 'pop-in' were observed for single crystal MgO, polycrystalline Al and polycrystalline SiC films on Si substrate. For bulk crystalline materials, the main 'pop-in' mechanism was associated with dislocation nucleation and its movement while for polycrystalline SiC films, it appears that nucleation of nanocrack is the dominant mechanism responsible for the 'pop-in'. The relationships between the 'pop-in'-triggered AE signals and the damage mechanisms of 'pop-in' were analyzed in terms of the indenter tip radius, film thickness, and microstructure of the materials.

1. Introduction

The development of nanoindentation allowed the characterization of local properties of materials on the nanoscale [1] as well as the damage mechanisms of materials during nanocontacts [2]. Because of the test's simplicity and its ability to mechanically probe materials on the nanoscale it has been recently widely used [3]. Nanoindentation tests are associated with high indentation-induced stress and stress gradients around the indenter tip, which can complicate the material's deformation and damage processes.

In nanoindentation tests some materials produce single or multiple sudden displacement excursions in their loading curves, i.e. indentation displacement suddenly increases while the normal load is kept constant. This phenomenon is commonly referred to as 'pop-in'. Since 'pop-in' is a fundamental and small-scale deformation behavior of a material, a careful investigation into it could potentially give insights into the mechanisms of microplasticity and microcracking and could contribute to the understanding of contact wear [4], fatigue and tribology in the small scale [5].

In the last decade, many researchers have made efforts to study the deformation mechanisms of 'pop-in'. Indentation-initiated 'pop-in' phenomena were observed in single crystal bulk materials such as Fe–3% Si, W [6], Au [7], MgO [8], Sapphire, 6H-SiC [4] and Ni_3Al(Cr,B) [9]. In these materials, 'pop-in' was generally thought to be associated with the onset of microplasticity, i.e. dislocation nucleation and the propagation of interstitial loops of dislocations beneath the indenter. This belief was

directly evidenced by TEM [4, 8]. ‘Pop-in’ was also found in layered single PbI_2 crystal [10]. By using an energy balance approach, the authors attributed this ‘pop-in’ to the creation and movement of extra dislocation layers.

Indentations on film-substrate system have shown ‘Pop-in’ phenomena as well. Weppelmann and Swain [11] found ‘pop-ins’ in 3.5 μm TiAlN films on stainless steel under indentation loads of 220 mN with a blunt tip (tip radius=35 μm). Berasategui and Page [12] observed multiple ‘pop-ins’ in the loading curves of epitaxial, cubic (3C)-SiC coatings on both (100) and (111) Si substrates at normal loads above ~40 mN. ‘Pop-in’ was found on CVD SiC films on (111) Si substrate with a normal load around 10 mN [13]. Amorphous hydrogenated carbon (a-C:H) films showed ‘pop-ins’ in the load range of 115 to 148 mN [14]. The ‘pop-in’ phenomena in the above film-substrate systems (i.e. a hard film on a soft substrate under a high normal load) were correlated to through thickness cracks and film delamination with the help of SEM. Knight et al. [15] suggested that the ‘pop-in’ represented the propagation of various types of cracks which locally relaxed membrane or residual stresses. These membrane stresses partly supported the indenter load, and their relaxation caused the indenter to move to a larger displacement, hence, creating the observed ‘pop-in’.

TiC_p reinforced Ni alloy coatings on steel substrates also showed ‘pop-in’ in the loading curves. This ‘pop-in’ was thought to indicate either the onset of plastic deformation of crack formation or TiC_p debonding from the matrix [16]. Interfacial fracture (delamination) induced ‘pop-in’ was observed with 500 nm thick Ti_2N film on sapphire

substrate, under a normal load of 210 mN with a blunt tip with radius of 1 μm [17]. Three independent delamination mechanisms were used to calculate the interfacial toughness. Despite the growing interests in the nanoindentation of thin film-substrate systems, very little is presently known about the microscopic deformation processes occurring beneath the indenter and their effects on the overall indentation response, especially the effects of film thickness, indenter tip radius and microstructure on the mechanisms of indentation-induced 'pop-in'. Therefore, these processes and effects, shown during nanoindentation, need further investigation with the help of other methods, which are capable of identifying highly localized deformation.

Acoustic emission (AE) is the transient elastic waves that are released inside a material that experiences abrupt changes in stress or strain. It is often expected that the measurement of a physical event using AE would allow an *in-situ* identification of both the magnitude and type of the event. As an important nondestructive testing technique, AE has been widely used for damage detection and identification [18]

Two types of pulse shaped AE signals were observed under the three point impact bending test by Richter [19]. One type of bursts which was characterized by short durations and high amplitudes, was thought to be a result of sound reflections from the unstable contact between the specimen and impact hammer. The other signal type, with comparably longer duration and lower amplitudes, was thought to indicate the beginning of a ductile crack extension. It should be noted that for large scale testing (as opposed to nanoindentation), multiple simultaneous events of plasticity or fracture contribute to a

cumulative AE. This provides AE levels sufficient for detection, but it does not allow one to associate the AE signal with the multiple events.

Nanoindentation is an operation mode with minimum background noise because there are no vibrations or friction noise from lateral movement. Therefore, it is an appropriate test for detection and identification of microdamage which usually has a low signal-to-noise ratio [20]. However, the number of dislocations or microcrack activities involved in highly localized deformation in a nanoindentation contact is very insignificant, and only a very small amount of energy is emitted in such tests, which requires higher AE detection resolution.

Therefore, such a nanoindentation test coupled with a highly sensitive AE detection is ideal. Recently commercial AE sensors have been used in conjunction with nanoindentation techniques to measure the *in-situ* indentation response of materials [21, 22]. Since nanoindentation could cause discrete and localized AE events, the ability to identify these physical events and correlate each event to the corresponding AE signal would give invaluable information on the deformation and damage mechanisms. For example, sharp changes in AE counts found in TiN films on sapphire, corresponding to the onset of 'pop-in' during indentation, can be related to the cracking and twinning of the sapphire [21]. In the indentation tests of platelet reinforced ceramics, From, et al. [22], found a clear distinction between the length of the indentation-induced cracks in the matrix material and those in the composite by analyzing the AE energy. In the above

conventional AE indentation tests, AE sensors were usually attached underneath the sample or close to the sample.

Undeniably, AE monitoring during an indentation can provide an extra insight into microscopic damage processes such as defect nucleation. However, since AE signals come from relatively low energy events, such as dislocation or crack nucleation, the captured AE energy might be below the resolution limit if an AE sensor is positioned some distance away from these event sites, as in the usual cases in the conventional AE monitoring indentation. Clearly, the placement of the sensor affects captured AE signals. In general, the detected AE signals were affected by the specimens' geometry [23], the sensor location and the sensor characteristics [24]. These factors caused difficulties in comparing data between various experiments.

Therefore, a standardized test environment needs to be controlled. With the recently developed Hysitron TriboAE^{TM} [25], AE signals can be sampled in the vicinity of the indentation contact area. As a result, sensitivity to highly localized nanoindentation induced microdamage events is increased [26]. It has been proved that the AE waveforms capture by TriboAE^{TM} were essentially independent of specimens' geometries. Hence TriboAE^{TM} could provide more reliable information and a consistent basis for an advanced quantitative analysis of physical processes.

The aim of this paper is to find the damage mechanisms of 'pop-in' for both bulk crystalline materials and film-substrate systems during nanoindentation under the *in-situ*

monitoring of AE. For this purpose, systematic AE monitoring nanoindentation tests were conducted on single crystal MgO, polycrystalline Al and polycrystalline SiC films deposited on Si substrates. Efforts were made to explore the relationships between an AE signal and the type and magnitude of an event that triggered the AE. Emphasis will be on comparing the 'pop-in' mechanisms for bulk crystalline material and film-substrate systems and analyzing the effects of indenter tip radius, film thickness, and microstructure on the mechanisms of indentation-induced 'pop-in'.

2. EXPERIMENTAL PROCEDURES

2.1. Specimens

MgO samples were prepared by cleaving single crystal bulk MgO along (001) crystallographic planes. The procedure resulted in smooth surfaces with multiple terraces up to several tens of microns wide as previously observed by Sangwal *et a*l. [27].

Highly pure (99.999%) aluminum foil (Goodfellow, Inc) has polycrystalline structure and a thickness of 0.1 mm. After surface cleaning with acetone, the foil was put in a mixture of 60 wt% perchloric acid and ethanol ($HClO_4$: C_2H_5OH= 1: 4 by volume), and then electropolished under a constant voltage of 3.5 V at room temperature for 10 minutes, with aluminum as the anode and copper plate as the cathode [28].

Recently, a new method for fabricating SiC films on single crystal Si (100) by chemical vapor deposition (CVD) was developed [29]. This new method, technically simple to

perform, has been proved to be able to produce polycrystalline SiC films with promising mechanical properties [30]. The SiC film is also able to be patterned using SiO_2 masking and a lift-off with HF. This makes it very promising for MEMS application.

All the SiC films were deposited on (100) Si substrate with the same deposition conditions: H_2 flow rate 75 sccm, SiH_4:CH_4=1:1, mixture flow rate of the precursor gases=1.44, presssure=25 mTorr and microwave power=720 W at the substrate temperature of 800^{o}C. In order to assess the influence of the film thickness on the damage process, SiC films were deposited by precisely controlling deposition time, which was in the range of 30 seconds to 25 minutes. Under these deposition conditions, the SiC film thickness *h*, determined by profilometry, was found to be in the range of 50-1355 nm.

2.2 AE indentation

The AE monitoring nanoindentation system(TriboAE^{TM}) shown schematically in Figure 1 consists of a nanoindentation instrument (TriboScope, Hysitron Inc.), a SPM/AFM scanner (NanoScope Ⅲ, Digital Instuments Co.), an AE sensor, an AE signal conditioner, a Digital Signal Processing (DSP) driven ADC/DAC base data acquisition system and a dedicated software.

The AE signals received at the AE sensor were amplified by 60 dB with a broad band signal conditioner followed by the 100-2000 kHz digital filter. To monitor the AE events continuously during quasi-static nanoindentation, AE data acquisition (sampling

frequency 10 MHz) was synchronized with the load/displacement data acquisition (sampling frequency 100 kHz) via two synchronized ADC/DAC/DSP 16-bit resolution boards. The synchronization was operated in a pre-triggering mode to ensure detailed waveform recording without cutting off the front of a signal. Due to the high AE data acquisition sampling frequency, burst type AE signals can be captured during a load/displacement data acquisition.

The trigger level for the AE data acquisition channel was set at 68 dB, based on the calculation of the system noise floor (NF), to avoid contamination of the signals by electronic and mechanical noises inherent in the system. The adjusted threshold for the AE monitoring was obtained by adjusting the trigger level until there was no AE event during an air indentation. For our test environment, the adjusted threshold was found to be between 69 and 70 dB.

The capacitive force-displacement transducer replaces the original cantilever of the AFM and is interfaced with detector assembly, signal adapter, and controller with dedicated software, thus enabling the application and sensing of normal forces in a controlled fashion. Details of the SPM instrument can be found elsewhere [31]. Nanoindentation experiments were performed with triangle-based pyramid-shaped (cube corner) diamond indenters with nominal radii of curvature equal to 116 nm and 685 nm. These indenter tips were mounted into the tip holder along with the miniature AE sensor (bandwidth 2 MHz) [26]. Quasi-static displacement and force resolutions are 0.1 nm and 1 nN, respectively. Tuning of the electrostatic force constant of the transducer and tip shape

calibration were carried out before testing. Tip calibration was based on the method of Oliver and Pharr [32]. To determine the tip-shape function, indentations of different contact depths were produced on fused quartz of hardness and elastic modulus approximately equal to 10 and 73 GPa, respectively. The hardness and elastic modulus of the films were calculated using the contact depth at maximum load and the slope of the unloading portion of the force-displacement curve determined near maximum load, respectively. Additional information about the tip shape calibration method and testing procedure used in the nanoindentation experiments can be found in previous publications [31, 32].

The loading history was set such that the applied load ramped linearly from zero to the maximum value in 5 s and was then relieved in 5 s, except as otherwise indicated. Various load indentations were located 2 microns apart to prevent the interaction of different indentations.

3. Results

3.1 Single crystal MgO

Figure 2 (a) shows a typical loading-unloading curve of nanoindentation in single crystal MgO with 685 nm radius tip, and Fig 2 (b) shows the captured AE signal corresponding to the AE event shown in Fig 2 (a). For elastic contact of two spherical elastic bodies, normal load can be related to the displacement between remote points in the bodies by [33]

$$p = \frac{4}{3} E^* \sqrt{Rh^3} \tag{1}$$

where p is the normal load, h is the normal displacement, E^* is the effective elastic modulus given by $E^* = \left[\left(1-\nu_1^2\right)/E_1 + \left(1-\nu_2^2\right)/E_2\right]^{-1}$, and R is the effective radius of curvature given by $R = \left[1/R_1 + 1/R_2\right]^{-1}$, where subscripts 1 and 2 denote the two contacting surfaces. The Hertzian elastic prediction, using $E^*_{MgO} = 317.17$ GPa and R=685 nm, coincided very well with the loading curve before 'pop-in'. The coincidence indicated that the deformation of the single crystal MgO was elastic at the early stage of the loading process. This is also evidenced by the SPM images which did not show any impression on the MgO surface when the normal load was withdrawn before 'pop-in'. When the normal load increased to $3068\mu N$, a 'pop-in' suddenly occurred with a burst type AE event captured, and the normal displacement jumped from 42.8 nm to 80.6 nm with the normal load kept as a constant. Hereafter, the normal load and the normal displacement associated with the onset of the 'pop-in' will be referred to as *critical load* p_{cr} and *critical displacemen* h_{cr} respectively. The distance over the displacement excursion will be referred to as *excursion length* δ, as shown in Fig 2 (a). After that the loading curve began to deviate from the elastic loading curve, as shown in the Fig 2 (a). The deviation indicated that the single crystal MgO continued to deform both elastically and plastically. The captured AE signal showed a steep rise from the system noise to the maximum amplitude (25424 micro volt) in a very short time (2.6 μs) which was followed by a rapid exponential attenuation extending over less than 30 μs, a typical characteristic of a damped oscillator. Some modulation of the decay suggested minor electronic and mechanical system instabilities or echo effects.

3.2 Polycrystalline Al

Two load-depth records from the nanoindentation into the polycrystalline Al foil, with the maximum normal loading set to $350\mu N$ and $450\mu N$ are shown in Fig. 3(a) with the corresponding AE waveforms captured shown in Fig. 3(b), (c), and (d). Corresponding elastic contact prediction by Eq 1, with R=685 nm and $E^*_{Al} = 64.43$ Gpa, was also shown in the above figure. Multiple 'pop-ins' were observed in both loading curves. One burst type AE event (event 1) was captured on the $350\mu N$ loading curve and two AE events (events 2 and 3) were captured on the $450\mu N$ loading curve. Larger amplitudes of AE event 1 and 2, which were accompanied with the first 'pop-in' on $350\mu N$ and $450\mu N$ loading curves, respectively, indicated that they were stronger than AE event 3 which occurred with one of the subsequent 'pop-ins' on the $450\mu N$ loading curve. Although the *critical load* and *excursion length*s were quite different (sensitive to the degree of surface roughness), both of the load curves before the first 'pop-in' were purely elastic (overlap each other). This claim was confirmed by directly imaging the surface before and after indentation with the same indenter. The unloading segment was more or less vertical, indicating that the elastic strains during indentation were small compared with the plastic strains, resulting in little elastic recovery. Moreover, the initial unloading slope was slightly negative which was due to the significant creep that occurred for polycrystalline Al. Similar phenomena were also observed for well-annealed Au surfaces [7]. The loading curve of polycrystalline Al with the 116 nm radius tip also showed

multiple ‘pop-ins’. However the *critical load* for the first ‘pop-in’ was only around 30 μN which was too low to initiate any AE signal to be captured.

3.3 SiC film on Si substrate

Table 1 shows the mechanical properties of the SiC films with different thickness. It is interesting to see that the hardness values increase with film thickness for thinner films (h<200 nm) and decrease with film thickness for thicker films (h>200 nm). ‘Pop-in’ was observed in the loading curves of SiC films with thickness in the range of 206 to 285 nm. Figure 4 (a) shows a typical load-unload curve of a 264 nm thick polycrystalline SiC film which was deposited on Si substrate, with the maximum normal loading set to $8000\mu N$ together with the corresponding elastic prediction by Eq 1 with R=685 nm and E^*=284.1 GPa, and a typical load-unload curve of the Si substrate material with the same tip. The captured AE signal is shown in Figure 4 (b). It was noticed that before the ‘pop-in’, the loading curve had already started to deviate from the elastic prediction. This deviation might be due to the plastic deformation of either the SiC film or Si substrate, microcrack nucleation inside the brittle SiC film or other microdamage processes. When the normal load increased to $6876\mu N$, a short, but clear, displacement excursion suddenly occurred with a burst type AE event captured and the normal displacement jumped from 105.49 to 107.81 nm. The obvious difference between the unloading curve shape of SiC film and that of Si substrate shown in Fig 4 (a) indicates that the majority of the SiC films could still support the load even after the ‘pop-in’.

In the indentation tests on TiN films, [34] where the AE sensor was mounted directly under the sample with cyanoacrylate glue, the burst type AE signal was found to have an amplitude within 20 μV, which is much smaller than the AE signal amplitude captured by TriboAE^{TM} as shown in Fig 4 (b) indicating the high sensitivity of TriboAE^{TM}.

Figure 5 shows *critical loads* of polycrystalline SiC films as a function of film thickness. It is clearly seen that the thicker the film, the larger the normal *critical load* needed to initiate 'pop-in'. Moreover, the *critical load* with the 116 nm radius tip was much lower than that with the 685 nm radius tip. Due to their similar mechanical properties as shown in Table 1, the *critical displacement* was observed to have similar trend with various SiC film thicknesses as shown in Fig 6.

Figure 7 shows the *excursion lengths* as a function of SiC films thickness. It is interesting to see that the thicker films generally gave longer *excursion length*s. The 206 nm, 240nm, 255nm thick samples showed similar *excursion lengths* initiated by the 116 nm and 685 nm radius tips. For the 264 nm, 285 nm thick samples, the *excursion lengths* with the 685 nm radius tip was larger than that with the 116 nm radius tip.

4. Discussion

4.1 Single crystal MgO

Figure 8 shows hardness values of single crystal MgO measured with the 116 nm radius tip, as a function of normal displacement. It is seen that the hardness increased with normal displacement, until it reaches a maximum value of 28.2 GPa at point A, and then it suddenly dropped down to a much lower value (14.8 GPa). The transition point A was found to correspond to the onset of 'pop-in' shown in Fig 2 (a). This indicates that the reason for the fall in the hardness values is that the penetration resistance changes from being elasticity-controlled to plasticity-controlled [4]. In nanoindentation tests, the values of hardness calculated by the maximum load over the corresponding contact area [32] are often found to change with penetration depth rather than being a material constant. However, the hardness values, defined by $P/\pi c^2$, where the plastic zone size c was obtained as the distance from the indent center to the dislocation farthest away from the indent as determined from the TEM images, were found to be roughly a constant and seemed to be a good measure of the material constant governing plasticity [9].

It has been shown in the previous section that the 'pop-in' on the loading curve of single crystal MgO corresponds to the first stage of irreversible deformation. This fact was thought to be relative to interstitial dislocation loops nucleation in [8]. After the 'pop-in', the loading curve develops in an elastic–plastic manner. The shape of the load depth curve is related to the elastic properties, the plastic flow behavior of the material and the tip geometry. This elastic-plastic process was found here to be responsible for the formation of the rosette arms pattern, as shown in Fig 9. This pattern is consistent with the cross slip of dislocations from underneath the indenter tip back to the free surface [8].

For crystalline materials, Bahr et al, [6] suggested that the *excursion length* could be related to the number of dislocations generated underneath an indenter. By assuming that the maximum change in shear stress over the 'pop-in' is the difference between the maximum shear stress under an elastic contact and the bulk shear flow stress of the material, the expression for *excursion length* in terms of *critical load* in [6] can be written as

$$\delta_{excursion} = \beta \frac{\tan\theta}{4G}\sqrt{\frac{3}{2\pi\sqrt{3}}}\left(0.31\left(\frac{6E^{*2}}{\pi^3 R^2}\right)^{1/3} P_{cr}^{\ 5/6}\tau_f^{-1/2} - P_{cr}^{\ 1/2}\tau_f^{1/2}\right) \quad (2)$$

where 1/ β is the fraction of dislocations that contribute to the tip displacement, G is the shear modulus, E^* and R are defined in the same manner as in section 3.1, and the dislocation movement flow angle θ from the indentation direction was assumed to be 35.4^o in [6]. The shear flow stress was given by

$$\tau_f = \frac{1}{\sqrt{3}}\sigma_{yield\ stress}\ (Von\ Mises\ criteria) \quad (3)$$

Figure 10 shows the *excursion length* as a function of *critical load* after taking E^*=317.2 GPa, R=685 nm, G=148 GPa and τ_f=80 MPa used in [35]. The fair agreement between analytical and experimental data indicates that dislocation nucleation is likely the dominant mechanism of 'pop-in' of single crystal MgO.

Figure 11 (a) shows a typical load-unload curve of nanoindentation in single crystal MgO with the 116 nm radius tip, and Fig 11 (b) shows the captured AE signal corresponding to the AE event shown in Fig 11 (a). Comparing this with the AE signal initiated by the 685 nm tip, we found that the AE signal with the 116 nm tip is order of magnitude weaker.

The AE characteristics for both tips are summarized in Table 2. It is not surprising to see that the *critical load* with the 685 nm radius tip is larger than that with the 116 nm radius tip. This is because the sharper tip can initiate larger shear flow stress in the material, thus making 'pop-in' occur at a lower *critical load*, and hence at a shorter *excursion lengths*. With smaller *excursion length*, the captured AE energy calculated by Eq (A. 1) is also found to be much weaker.

4.2 Polycrystalline Al

4.2.1. Stair-case 'pop-ins'

Aluminum showed elastic deformation and a nanoindentation-induced 'pop-in' at the early stages of the loading process similar to the single crystal MgO. However stair-case 'pop-ins' followed the first displacement excursion as shown in Fig 3 (a), rather than a continuous elastic-plastic deformation.

The continuous lines in Fig 12 were drawn based on Eq. 1 after choosing E^* to be 64.43 GPa. This effectively translated the purely elastic loading curves along the normal depth axis. The coincidence between translated elastic prediction and the subsequent loading curve after the first 'pop-in' indicates that in-between the displacement bursts, the indentation response was an offset of the Hertzian curve and was determined solely by the elastic properties of the film. It is hence concluded that the overall nanoindentation response of polycrystalline Al is comprised of two parts: purely elastic deformation and

an intermittent, microplasticity which is characterized by discrete ‘pop-ins’ in the loading curve.

Single crystal MgO could sustain high elastic stress approaching the theoretical shear stress. At the ‘pop-in’, a dislocation avalanche was initiated, and many dislocations were created so that the sample had a larger number of sources to continue to accommodate plastic deformation until the loading curve reached the geometrically necessary loading shape, as shown in Fig 2 (a). While for polycrystalline Al, only a few dislocations were emitted at the first ‘pop-in’. After that the tip was no longer in elastic contact with the sample. Therefore, the stress driving the dislocations dropped dramatically. Later, an equilibrium was set up between the dislocations and the indenter. The equilibrium made the indenter behave as if it were in an elastic medium as shown in Fig 12. If the driving stress was low enough, the sample again would elastically load until the shear stress was high enough to activate the next ‘pop-in’ [6]. In another words, the dislocation activities nucleated at the first pop-in of polycrystalline Al were unable to sustain plastic deformation without more dislocation nucleation occurring. Although multiple ‘pop-ins’ were needed to accommodate the tip penetration, the amount of the energy released with each ‘pop-in’ was different. The *excursion lengths* of most of the first ‘pop-ins’ were found to be longer than those of the subsequent ‘pop-ins’. Since AE energy is believed to be proportional to the *excursion lengths* [36], it is not surprising to see that the first ‘pop-in’ always gives larger energy than those released by the subsequent ‘pop-ins’, as shown in Fig. 13. Actually for most subsequent ‘pop-in’ cases, the energy released was so weak that no AE signal could be captured.

The *critical load* for the first 'pop-in' varied for different indentations due to the surface roughness effect etc, but after the excursion the loading curves followed the same geometrically necessary curve, as shown in Fig. 3 (a). The accompanying rotation of the lattice was manifested as material pile-up around the sharp cube-corner indentation, observed by SPM images of indented Al films, as shown in Fig 14. TEM monitoring indentation on Al films proved that geometrically necessary dislocations nucleated beneath the indenter tip to accommodate the shape change imposed in the material by the indenter [37].

It is interesting to note that before electropolishing, no 'pop-in' could be found in any loading curve of the polycrystalline Al samples. Similar observations on Single <111> NiAl and singal crystal W were found [3]. The high density of pre-existing dislocations in the surface region due to the mechanical rolling process during manufacturing [38] might be responsible for this. This pre-existing dislocation can hinder the additional dislocation activities required for initiating 'pop-in' under indentation. It was also noticed that the loading curves of the pre-electropolished surfaces were consistently above the electropolished curves after the 'pop-in', as shown in Fig 15. This again showed the dislocation density effect on the nanoindentation response of polycrystalline Al.

4.2.2. Time dependent pop-in'

As discussed before, a 'pop-in' could be initiated when the normal load exceeds the *critical load*. However, we found that polycrystalline Al also generated 'pop-ins' when

the normal load was lower than the *critical load* provided that the normal load was held for a certain time. Figure 16 (a) shows a load-unload curve for polycrystalline Al with the 685 nm radius tip. The maximum load was set to 80 μN, which was lower than the *critical load* for polycrystalline Al with this tip (~105 μN). After holding the tip with the maximum load for 75 seconds, the normal displacement suddenly increased from 83.42 nm 206.29 nm, with a burst type AE signal captured as shown in Fig 16 (b). Due to the creep behavior of the material, a portion of the load was absorbed by the springs of the transducer during the load holding period and hence caused the normal load to drop throughout the load holding.

The waiting time before 'pop-in' was found to increase from 5.45 ± 1.3 seconds to 80.5 ± 22 seconds as the holding load decreased from 90 μN to 80 μN. No 'pop-in' could be detected when the holding load was lower than 80 μN because of the holding time limitation of the indentation system. Time-dependent 'pop-in' was also found for Fe±3 wt% Si single crystal in [39] and Ni_3Al single crystal in [40]. This phenomenon was thought to be caused by the transition from a stable dislocation loop, which was nucleated underneath the indenter tip, to an unstable loop [40]. When the unstable loop size was reached, the loop expanded catastrophically activating a 'pop-in' in the loading curve. Figure 17 shows that the calculated AE energy increased with waiting time. This indicated that the more time the stable dislocation loop needs to reach the unstable loop size, the more elastic energy the material stores before 'pop-in' and releases during the 'pop-in'. Hence more AE energy could be captured correspondingly.

In the foregoing discussions, ‘pop-in’ of polycrystalline Al was thought to be caused by dislocation nucleation rather than oxide layer breaking. This assumption is supported by the following observations:

1. Multiple displacement bursts were observed in polycrystalline Al foil even at penetration depths significantly larger than those corresponding to the thickness of an amorphous oxide layer on the surface, which is expected to be of the order of 5–10 nm [41]. Also time-dependent ‘pop-in’ was initiated at an even deeper penetration depths than the amorphous oxide thickness, as shown in Fig. 16 (a).

2. Nanoindentation on noble metals such as Au, which is free of any surface oxides or contamination layers, also showed reproducible ‘pop-ins’ in its loading curve during nanoindentations [7].

3. It was found that the *critical load* depended heavily on the crystal orientation, although crystal orientation did not dramatically alter the oxide characteristics [4, 7, 42] This is because altering crystal orientation changes the resolved shear stresses underneath the indenter tip.

4. In the previous discussion it was noted that the ‘pop-in’ did not occur on polycrystalline Al before it was electropolished, which would also be covered by thin oxide layer.

In view of these experimental observations, it is concluded that while native oxide layers could influence the nanoindentation response in the very early stages of loading, any cracking of such protective layers did not appear to be the controlling mechanism responsible for the 'pop-in' of polycrystalline Al.

4.3. Polycrystalline SiC film on Si substrate.

To study the thin film-substrate system one needs to understand the substrate response first. A series of nanoindentation tests were performed on single crystal Si (100). However, no 'pop-in' was observed throughout the tests, and this suggested that dislocation nucleation did not control plastic deformation in this material. On the other hand, 'pop-out' phenomenon was seen in the unloading curve of single crystal Si, as indicated by point B in Fig 4 (a). The plasticity of Si is thought to arise from a densification transformation (response to the high hydrostatic compression under an indenter) [4], while the 'pop-out' was correlated with the corresponding undensification process [43]. As reported there, during loading the Si1 cubic diamond structure transformed into a 27% denser Si2 tin-like structure, and during unloading, it returned to a new cubic Si3 phase which was only 8% denser than the initial diamond structure.

4.3.1 'Pop-in' mechanism

Figure 18 shows the AE energy, calculated by Eq (A.1), as a function of the *excursion length*s for single crystal MgO, polycrystalline Al and 285 nm thick polycrystalline SiC film, with 685 nm radius tip. From this log plot it is seen that the AE energy increased with *excursion length* for all the materials. This observation is similar to the results in

[36], which proved experimentally that the AE energy was proportional to δ^2 for tungsten (001) single crystal. The relation between the measured AE energy and the *excursion length* of 'pop-in' implies the feasibility of detecting and identifying the damage processes during nanoindentation. Bulk crystalline MgO and Al showed longer *excursion length*s than the polycrystalline SiC film. Single crystal MgO gave the largest AE energy due to the dislocation avalanche occurring with the 'pop-in'. While for polycrystalline material, the movement of dislocations or microcracks is restricted by the grain boundaries, and it is harder to trigger the dislocation avalanche than in single crystal MgO. Though polycrystalline SiC films showed much shorter *excursion length*s than the polycrystalline Al, they offered the same scale of AE energy as the polycrystalline Al. This indicates that the 'pop-in' mechanism of polycrystalline SiC films might be different from that of polycrystalline Al, i.e. dislocation nucleation might not be the dominant mechanism for 'pop-in' in polycrystalline SiC films. The SPM images of the polycrystalline SiC film in Fig 19 were taken before and after a nanoindentation. In Fig 19 we did not observe any obvious pile up around the indenter tip that accompanied dislocation nucleation and its movement back to the free surface, as shown in Figs 9 and 14.

The theoretical shear strength of a material may be approximated as $G/2\pi$ and the maximum shear stress inside materials can be calculated by using Herzian contact theory as [33]

$$\tau_{\max} = 0.31\left(\frac{6P_{cr}E^{*2}}{\pi^3 R^2}\right)^{1/3} \tag{4}$$

where E^* and R are defined in the same manner as in section 3.1. Table 3 lists the values of theoretical shear strength and maximum shear stress for different materials. In light of bulk crystalline materials, i.e. single crystal MgO and polycrystalline Al, the comparison results shown in Table. 3. supports the view that the first 'pop-in' of these two bulk crystalline materials occurred when the maximum shear stress beneath the indenter approached the theoretical shear stress. This offers a physical justification for the nucleation of dislocations following the initial elastic indentation response. However, for polycrystalline SiC films, the maximum shear stress beneath the indenter at the 'pop-in' was only a third of the theoretical shear stress. This fact suggests that shear stress-driven dislocation plastic deformation might not be the dominant cause of the 'pop-in' in the loading curve of polycrystalline SiC films.

For polycrystalline materials, dislocations often pile up against the grain boundaries and are characterized by large stress concentrations close to the pile up. There are two possible mechanisms to release this stress. One is the pileup dislocation penetrating through the grain boundaries, and the other is crack nucleation. Both of the methods are accompanied by rapid release of the stored elastic energy. [24, 44]

TEM observation of (0001) single crystal sapphire gave direct evident of indentation-induced nanocrack nuclei. These cracks were thought to be stable until a sufficiently large strain energy density was created to make the growth energetically favorable at a higher load [4]. Mircoracks along the columnar grain boundaries of TiN film were observed by SEM [21]. A significant increase in AE counts was correlated to the 'pop-

in'. This suggests that shear faulting of the film contributes to the irreversible deformation of TiN film rather than to dislocation movement.

Cross-section TEM images showed that the mircostructure of the SiC film consisted of a 3-5 nm thick, epitaxial 3C-SiC layer, followed by columnar 3C-SiC grains [45]. During the growth competition following the nucleation, the slower growing grains were overgrown by the faster growing grains. Therefore, the grains were aligned with their fastest growth direction normal to the substrate, creating columnar grains [46], which was the common microstructure of ceramic films [47]. Since the grain sizes of SiC films used in these tests were only in the range of 40-60 nm, as observed by TEM cross-sectional image [45], several surface grains, including their grain boundaries, were deformed under the indenter tip during an indentation. This process enhanced the possibility of crack nucleation, in the range of nano or micrometers length scales, along the grain boundaries. Actually due to the highly hardness and brittle features of the SiC films, they lack the capability to sustain large plastic strains, to adapt themselves to the diamond indenter tip's geometry. Under higher load these nanoindention-induced microcracks grow along cylindrical grain boundary surfaces through the thickness of the film. This growth was thought to be a natural occurrence in films having a columnar grain structure with the axes of the elongated grains being perpendicular to the film surface [48]. Also SiC films deposited at 800^{o}C were found to have tensile residual stress [46], which would help the nucleated crack to propagate along a grain boundary. It should be noted that the residual stress effect in these films was overshadowed by the effects owing to the indentation-induced stress.

The foregoing discussions indicate that for brittle SiC films with columnar microstructure, nucleation of nanocracks may be one of the dominant mechanisms responsible for the 'pop-in', despite the fact that dislocation movement might contribute to it. It is generally believed that `pop-ins' with low *critical loads* (<1 mN) are often associated with dislocation nucleation events in bulk crystalline material. `Pop-ins' at higher loads in coated systems were more likely to be caused by nucleation of nanocracks [12].

Considering the strength and durability of polycrystalline SiC films, fracture toughness is one of their most important characteristics due to their high brittleness. The strain energy release rate G can be defined by [49]

$$G = -\frac{1}{2\pi c}\left(\frac{dU}{dc}\right) \tag{5}$$

where c is the crack length and U is the strain energy released to create new crack surfaces. From the presented discussions, we know that the nanoindentation-induced crack should be Mode I fracture dominated. Since no pile up around the indenter tip was observed, we assumed that indentation-induced volume change only resulted in expansion of the film in the plane parallel to the film surface (plane strain status). The relationship between the strain energy release rate and the fracture toughness under plane strain condition can be expressed as

$$G = \frac{K_I^2}{\mathrm{E}}\left(1-\nu^2\right) \tag{6}$$

where K_I is the stress intensity factor in Mode I fracture, E is the Young's modulus of material and υ is the possion's ratio. After substituting Eq 5 into Eq 6, we reached

$$K_c = \left[\left(-\frac{E}{(1-\nu^2)2\pi c} \left(\frac{dU}{dc} \right) \right) \right]^{1/2} \tag{7}$$

Since the crack propagates very fast, we can regard it as a single event, i.e. $-\frac{dU}{dc} = \frac{U}{c}$.

To obtain the direct expression of the fracture toughness, we need to have two more assumptions. First we assume that the strain energy dissipated in an individual fracture can be expressed in terms of the magnitude of the 'pop-in', i.e. $U = P_{cr} \cdot \delta$. Secondly we assume that the crack length can be obtained by measuring the *excursion length*, i.e. $\delta = c$, although the *excursion length* of SiC films was usually only several nanometers (nanocrack). Hence after substituting U into Eq 6, we can write the fracture toughness as

$$K_c = \left[\frac{EP_{cr}}{(1-\nu^2)2\pi\delta} \right]^{1/2} \tag{8}$$

Figure 20 shows the fracture toughness of polycrystalline SiC film calculated by Eq 8 as a function of film thickness. It is seen that fracture toughness increased with film thickness, and hence increased with grain size since the size of the columnar SiC grain became larger as the film thickness increased [46]. For small grain size the dislocation movement would be inhibited and the critical stress would be high. So if dislocation movement was the dominant mechanism for 'pop-in' of polycrystalline SiC film, the *critical load* should decrease with increasing film thickness and grain size, which was disapproved by the experimental results shown in Fig 5. Recalling the hardness values listed in Table 1, we learned that the harder SiC film, the lower the fracture toughness. This relationship proved the general hardness to toughness relationship, i.e. higher hardness leads to lower toughness. It is noted that the fracture toughness of the

polycrystalline SiC films calculated by Eq. 8 were much higher than the values obtained through the conventional Vickers indentation method, which was only in the range of 4-7 $MPam^{1/2}$ [50]. This discrepancy indicates that the real crack length might be longer than the *excursion length*. Direct measurement of the crack length from TEM images, which is a very difficult task, is needed to obtain a better prediction.

The lower *critical load*s and *critical displacement*s of thinner SiC films (206 nm, 240 nm, and 255 nm), as shown in Fig 5 and Fig 6, were thought to be caused by their comparably lower fracture toughness. A similar trend in the thickness dependence of P_{cr} was found for single crystalline GaN films on sapphire [51], Single crystal Fe (3 wt. % Si) [5], and amorphous SiO_2 films [52].

The tougher properties of the thicker SiC films as compared with the thinner films were also exhibited in the higher AE energy, as shown in Fig. 21. This is because with larger *critical load* and *excursion length*, the thicker films could store more elastic energy before the 'pop-in' and hence release more energy during the nanocrack nucleation.

Tip radius effects were seen in Figs 5 to 7 and Fig 21. With the same normal load a sharper tip would cause higher local stress concentration. This fact made it easier to reach the *critical load* needed to initiate 'pop-in'. The *critical load* depends mainly on the indenter tip radius, although to a lesser degree, it was also dependent on the surface conditions, the composition microstructure of the film and the residual stress in the film. The tip radius effect on the *critical load* of 'pop-in' was also observed for Fe-3%Si single

crystal [53]. *Critical load*, with Berkovich tip with an apex radius of approximately 585 nm, was more than two times as large as that with a cube corner tip with a radius of approximately 265 nm.

4.3.2. Multiple 'pop-in' and AE events

It is worth noticing that for indentation of SiC films with thickness less than 200 nm (58 nm and 150 nm thick films), no 'pop-in' was initiated during any loading process. This is mainly because before reaching the *critical load* for 'pop-in' to occur, the tip had already penetrated into the Si substrate which did not show 'pop-in' phenomenon, as we discussed previously. Since the interfacial cracking or delamination, if any, which occurred in the horizontal direction did not greatly affect the normal displacement, it would not contribute to the 'pop-in' phenomenon. However they might initiate AE events. Figure 22(a) shows a loading curve for a 58 nm thick SiC film. Although there was no indentation-induced 'pop-in' on the loading curve, two AE events were captured, as shown in Figs 23 (b) and (c). Here the AE events were thought to be caused by the possible interfacial cracking or delamination for the very thin SiC film. Further evidence from high resolution microstructural studies by TEM is needed to confirm the above assertion. During the nanoindentation of a 1355 nm thick SiC film, no 'pop-in' was found, even when the normal load was increased to 8000 μN. This might due to the large toughness of the thick film. Recall that toughness increased with film thickness (>200 nm). The *critical load* for this film was thought to exceed the maximum load limitation of the system.

Two ‘pop-ins’ were sometimes observed in the loading curves of polycrystalline SiC film with 116 nm radius tip. Figure 23 (a) shows a load-unload curve for the 264 nm thick SiC film with 116 nm radius tip. There were two ‘pop-ins’ with two corresponding AE events successfully captured as shown in Fig 23(b) and (c). As the normal load increased, plastic deformation in the SiC substrate would increase, and the SiC film above the plastic deformation area of a substrate would have to bend to conform to the Si substrate deformation. This would resulte in tensile stress in the remaining parts of the film. When the stress intensity factor was larger than the fracture toughness of the SiC film, nucleation of nanocracks would occur corresponding to the first ‘pop-in’. The loading curve before and after the first ‘pop-in’ had similar shapes, which indicates that after the nanocrack nucleation corresponding to the first ‘pop-in’, the load-support capacity of the SiC film would not change very much.

With increasing load, plastic deformation in the substrate would reach a critical state. Delamination of the film might occur due to large strain mismatch at the film/substrate interface, and it could lead to relative motion between the SiC film and the Si substrate, hence resulting in the second ‘pop-in’. After the second ‘pop-in’, the slope of the loading curve became smaller, and the loading curve seemed to be distorted rather than maintaining its continuous shape. This observation indicates that the load-support capacity of the SiC film decreased outstanding due to the film delamination. It should be noted that both of the ‘pop-ins’ could not be caused by the fracture of the Si substrate as discussed before.

Although nanocracks nucleated during nanoindentation could be associated with the 'pop-in' of polycrystalline SiC films, they are not necessary to initiate 'pop-in' in the loading curve and for AE signals to be captured. Figure 24(a) shows a load-unload curve for a 285 nm thick SiC film with 116 nm radius tip. Three 'pop-ins' are seen in the loading curve. Two AE events were captured, accompanying the second and third 'pop-ins', as shown in Figs 24(b) and (c). These two 'pop-ins' which were thought to be caused by the relative motion of the delaminated parts of the film, were much less apparent than the first 'pop-in. However, no AE signal was triggered corresponding to the first 'pop-in' even though it had longer *excursion length* than that of the other two 'pop-ins' that followed.

Not only was it important to observe the magnitude of energy released, but also the energy release rate since it determines the amplitude of AE signal. For example, stable crack growth does not necessarily offer AE signals exceeding the system noise floor. Table 4 shows the statistics of the AE monitoring indentations on polycrystalline SiC films. For each indentation, generally there were three possible results: 1) the loading curve was continuous with no 'pop-in'; 2) there was 'pop-in' on the loading curve but no AE signal could be captured; 3) there was 'pop-in' on the loading curve and an AE signal could be captured corresponding to the 'pop-in'. For both tips we can see clearly that as the film thickness increased (within the range being considered), the possibility for the tip to initiate a 'pop-in' and the possibility to capture an AE signal both increased. As we know, SiC toughness increases with film thickness, so lower *critical load* was needed to initiate nanocracks for thinner films and hence caused shorter *excursion length*. The very

short *excursion length* would lower the possibility to observe 'pop-in' in the loading curve. Also the AE signals accompanying the 'pop-in' would be weaker accordingly for the thinner films. Therefore with the lower signal to noise level, it would be very difficult for the AE sensor to capture a AE signal.

5. Conclusions.

The damage mechanisms of 'pop-in' for both bulk crystalline materials and film-substrate system were investigated by performing nanoindentation tests using cube corner tips with nominal radii of curvature equal to 116 and 685 nm, under the *in-situ* monitoring of acoustic emission. The relationships between the 'pop-in'-induced AE signals from both bulk crystalline materials and film-substrate system and damage mechanisms of 'pop-in' were analyzed in terms of the effect of indenter tip radius, film thickness and microstructure of the materials. Based on the presented results and discussion, the following main conclusions can be drawn.

1. For bulk single crystal MgO and polycrystalline Al, the main mechanism for 'pop-in' is dislocation nucleation and movement. This was evidenced by both experimental results and theoretical prediction. On the other hand, for brittle polycrystalline SiC films with columnar microstructure, nucleation and propagation of nanocracks might be one of the dominant mechanisms responsible for the 'pop-in', although dislocation movement might also contribute to it.

2. The stair-case ‘pop-in’ was limited to cases where only a few nucleated dislocations were emitted at the first ‘pop-in’. This nucleated dislocations were unable to sustain plastic deformation without more dislocation nucleation occurring. The first ‘pop-in’ for polycrystalline Al always gave larger energy than the subsequent ‘pop-ins’. The single ‘pop-in’ cases for single crystal MgO, with a large excursion length, indicated that a dislocation avalanche was initiated and many dislocations were created so that the sample had a larger number of sources which would continue to accommodate plastic deformation, until the loading curve reached the geometrically necessary loading shape.

3. Time-dependent ‘pop-in’ was caused by the transition from a stable dislocation loop, nucleated underneath the indenter tip, to an unstable loop. A plot of AE energy .vs. waiting time indicated that the more time the stable dislocation loop needed to reach the unstable loop size, the more elastic energy the material could store before ‘pop-in’ and release during the ‘pop-in’.

4. ‘Pop-in’ was observed in the loading curves of polycrystalline SiC films with thickness in the range of 206 to 285 nm. C*ritical load* and *critical displacement* of polycrystalline SiC film increased with film thickness. *Critical load* with the 116 nm radius tip was much lower than it was with the 685 nm radius tip. Thicker films generally gave larger *excursion length*s and AE energy. With increasing film thickness, the possibility for the tip to initiate a ‘pop-in’ (film quality) and the possibility of capturing an AE signal both increased. The thickness dependence of film toughness was observed and used to explain the film thickness effect on the nanoindentation-induced ‘pop-in’.

5. AE events observed for thinner SiC films (<150 nm) were caused by the possible interfacial cracking or delamination.

6. Multiple 'pop-ins' were sometimes observed in the loading curves of polycrystalline SiC film with the 116 nm radius tip. The first 'pop-in', which might be associated with nucleation of nanocracks, was initiated when the stress intensity factor was larger than the fracture toughness of the SiC film. A subsequent 'pop-in' was caused by the relative motion between the SiC film and the Si substrate during possible delamination of the film. After the second 'pop-in', the slope of the loading curve became smaller and the loading curve seemed to be more lagged rather than substantially continuous. This indicated that the load-support capacity of the SiC film decreased a lot due to the film delamination.

7. Tip radius was found to have significant effects on *critical load, excursion length* and AE energy. Blunter tip could offer larger *critical load,* and hence triggered bigger *excursion length* and AE energy for both bulk crystalline materials and thin film-substrate system.

8. Finally, we concluded that monitoring the nanoindentation tests with AE did not contribute to our understanding of the 'pop-in' mechanisms. Energy is abruptly released with the 'pop-in' and it can sometimes be detected by the AE transducer integrated in the indentation tip holder. AE can often tell us that a 'pop-in' occurred but it is not as reliable in this regard as observation of the load-unload curve.

ACKNOWLEDGEMENT

First and foremost, I would like to thank my research advisor, Professor David B. Bogy, for his consistent support and guidance. His genuine respect for his students has been deeply appreciated by us. I also wish to thank Professor Kyriakos Komvopoulos for serving on my thesis committee and giving me valuable helps during my master research. I also want to thank the current members of CML for their support and the memorable moments we shared.

This work was supported by the Computer Mechanics Laboratory (CML) at the University of California at Berkeley. We extend many thanks to Hysitron, Inc. for providing the TriboAE^{TM} and to several members of the staff for installing and explaining the use of the TriboAE^{TM} system. I also thank Di G and Muthu B. J in Dept of Chemical engineering in UC Berkeley for providing the SiC film samples.

Appendix

Based on the amplitude of the AE sensor output, A(t), the AE energy can be calculated as

$$E_A(t) = \int_0^{t_a} A(t)^2 \, dt \qquad \text{(A.1)}$$

where t_a is the signal attenuation time for the AE signal amplitude to decay to the background level. This provides a meaningful measurement of the strength of an AE event. Although this is not a true energy since the resistance of the sensor and the

dissipation of the energy during propagation are not included. Details of the AE energy calculation can be found in [54].

REFERENCES

[1]. Chung-Jen Lu and D. B. Bogy, The effect of tip radius on nano-indentation hardness tests, International Journal of Solids and Structures, Volume 32, Issue 12, June (1995) 1759-1770.

[2]. X. G. Ma, K. Komvopoulos, D. J. Wan, D. B. Bogy and Y.-S. Kim. Effects of film thickness and contact load on nanotribological properties of sputtered amorphous carbon thin films, submitted (2003).

[3]. W. W. Gerberich, D. E. Kramer, N. I. Tymiak, A. A. Volinsky, D. F. Bahr and M. D. Kriese. Nanoindentation-induced defect–interface interactions: phenomena, methods and limitations, Acta Materialia, Volume 47, Issues 15-16, November (1999) 4115-4123.

[4]. T. F. Page, W. C. Oliver, and C. J. McHargue, The deformation behavior of ceramic crystals subjected to very low load (nano) indentations, J. Mater. Res. Vol 7. No. 2, (1992) 450-473.

[5]. S. K Venkataraman, D. L. Kohlstedt, and W. W. Gerberich, Continuous microindentation of passivating surface. J. Mater. Res. Vol. 8. No 4. (1993) 685-688.

[6]. D. F. Bahr, D. E. Kramer and W. W. Gerberich, Non-linear deformation mechanisms during nanoindentation, Acta Materialia, Volume 46, Issue 10, 12 June (1998) 3605-3617.

[7]. S. G. Corcoran, R. J. Colton, E. T. Lilleodden, and W. W. Gerberich, Anomalous plastic deformation at surfaces: Nanoindentation of gold single crystals, Phys. Rev. B 55, (1997) 57-60.

[8]. C. Tromas a , J. Colin, C. Coupeau, J.C. Girard, J. Woirgard, and J. Grilh_e, Pop-in phenomenon during nanoindentation in MgO, Eur. Phys. J. 8 (1999) 123-128.

[9]. Y. L. Chiu and A. H. W. Ngan, A TEM investigation on indentation plastic zones in $Ni_3Al(Cr,B)$ single crystals, Acta Materialia, Volume 50, Issue 10, 12 June (2002) 2677-2691.

[10]. W. Veiga and C. M. Lepienski, Nanomechanical properties of lead iodide (PbI_2) layered crystals, Materials Science and Engineering A, Volume 335, Issues 1-2, 25 September (2002) 6-13.

[11]. E. Weppelmann and M. V. Swain, Investigation of the stresses and stress intensity factors responsible for fracture of thin protective films during ultra-micro indentation tests with spherical indenters, Thin Solid Films, Volume 286, Issues 1-2, 30 September (1996) 111-121.

[12]. E. G. Berasategui and T. F. Page, The contact response of thin SiC-coated silicon systems—characterisation by nanoindentation, Surface and Coatings Technology, Volumes 163-164, 30 January (2003) 491-498.

[13]. A. J. Whitehead, and T. F. Page, Nanoindentation studies of thin film coadted systems, Thin solid films. 220, (1992) 277-283.

[14]. J. Qi, K. H. Lai, C. S. Lee, I. Bello, S. T. Lee, J. B. Luo and S. Z. Wen, Mechanical properties of a-C:H multilayer films, Diamond and Related Materials, Volume 10, Issues 9-10, September-October (2001) 1833-1838.

[15]. J. C. Knight, A. J. Whitehead, and T. F. Page, Nanoindentation experiments on some amorphous hydrogenated carbon (a-C:H) thin film on silicon, Journal of materials science, 27, (1992) 3939-3952.

[16]. Xiaolei Wu and Youshi Hong, Microstructure and mechanical properties at TiC_p/Ni-alloy interfaces in laser-synthesized coatings, Materials Science and Engineering A, Volume 318, Issues 1-2, November (2001) 15-21.

[17]. D. F. Bahr, J. W. Hoehn, N. R. Moody and W. W. Gerberich, Adhesion and acoustic emission analysis of failures in nitride films with a metal interlayer, Acta Materialia, Volume 45, Issue 12, December (1997) 5163-5175.

[18]. Sotirios J. Vahaviolos**,** Acoustic emission : standards and technology update , West Conshohocken, PA, (1999)

[19]. H. Richter, J. Böhmert and H. -W. Viehrig, The use of acoustic emission to determine characteristic dynamic strength and toughness properties of steel, Nuclear Engineering and Design, Volume 188, Issue 2, 2 April (1999) 241-254.

[20]. J. von Stebut, F. Lapostolle, M. Bucsa and H. Vallen, Acoustic emission monitoring of single cracking events and associated damage mechanism analysis in indentation and scratch testing, Surface and Coatings Technology, Volumes 116-119, September (1999) 160-171.

[21]. M. V. Swain and M. Wittling, Comparison of acoustic emission from pointed and spherical indentation of TiN films on silicon and sapphire, Surface and Coatings Technology, Volumes 76-77, Part 2, December (1995) 528-533.

[22]. P. S. From, B. Clausen, E. Ø. Nielsen and R. Pyrz, Indentation and acoustic emission in filtration processed platelet reinforced ceramics, (1995) 231-236

[23]. D. F. Bahr and W. W. Gerberich, Relationships between acoustic emission signals and physical phenomena during indentation, 13 (1998) 1065-1074.

[24]. A. Vinogradov, S. Hashimoto and S. Miura, Effect of grain boundary on acoustic emission during plastic deformation of copper-aluminum bicrystals, Acta Materialia, Volume 44, Issue 7, July (1996) 2883-2890.

[25]. A. Daugela, J. T. Wyrobek, Proc of Intermag, Toronto, April 9-13, (2000) HB03.

[26]. A. Daugela, H. Kutomi, T.J. Wyrobek, Nanoindentaion induced acoustic emission monitoring of native oxide fracture and phase transformations, Zeitschrift fur Metall., **9**2, (2001) 1052-1056.

[27]. K. Sangwal, P. Gorostiza, J. Servat, F. Sanz, Atomic force microscopy study of nanoindentation deformation and indentation size effect in MgO crystals, J. Mater. Res., Vol 14, No. 10. (1999) 3973-3982.

[28]. Jiayang Juang and David B. Bogy, Fabrication of Self-Assembled Nanoporous Templates for Applications to Patterned Media Recording, CML report (2003).

[29]. Conrad R. Stoldt, Carlo Carraro, W. Robert Ashurst, Di Gao, Roger T. Howe and Roya Maboudian,A low-temperature CVD process for silicon carbide MEMS, Sensors and Actuators A: Physical, Volumes 97-98, 1 April (2002) 410-415.

[30]. Stoldt CR, Fritz MC, Carraro C, Maboudian R, Micromechanical properties of silicon-carbide thin films deposited using single-source chemical-vapor deposition., Applied Physics Letters, vol.79, no.3, 16 July (2001) 347-349.

[31]. W. Lu, K. Komvopoulos, Nanotribological and nanomechanical properties of ultrathin amorphous carbon films synthesized by radio frequency sputtering, ASME Journal of Tribology 123 (2001) 641-650.

[32]. W. C. Oliver, G. M. Pharr, An improved technique for determining hardness and elastic modulus using load and displacement sensing indentation experiments, Journal of Materials Research 7 (1992) 1564–1583.

[33]. K. L. Johnson, Contact Mechanics, Cambridge University Press, Cambridge, UK. (1985).

[34]. M. Shiwa, E. R. Weppelmann, A. Bendeli, M. V. Swain, D. Munz and T. Kishi, Acoustic emission and precision force-displacement observations of spherical indentations into TiN films on silicon, Surface and Coatings Technology, Volumes 68-69, December (1994) 598-602.

[35]. K. Sangwal, F. Sanz and P. Gorostiza, Study of the surface morphology of the (100) cleavage planes of MgO single crystals by atomic force microscopy, Surface Science, Volume 424, Issue 1, 19 March (1999) 139-144.

[36]. Natalia. I. Tymiak, Ph.D. Thesis. (2000).

[37]. Eric A. Stach, Tony Freeman, Andrew M. Minor, Doug K. Owen, John Cumings, Mark A. Wall, Tomas Chraska, Robert Hull, J. W. Morris Jr., and Ulrich Dahmen, Development of a Nanoindenter for In-situ Transmission Electron Microscopy, Microscopy and Microanalysis, 7, (2001) 507-517.

[38]. A. Krell, A new look at the influences of load, grain size, and grain boundaries on the room temperature hardness of ceramics, International Journal of Refractory Metals and Hard Materials, Volume 16, Issues 4-6, (1998) 331-335.

[39]. W. W. Gerberich, D. E. Kramer, N. I. Tymiak, A. A. Volinsky, D. F. Bahr and M. D. Kriese, Nanoindentation induced defect-interface interactions: phenomena, methods and limitations, Acta mater. Vol. 47, (1999) 4115-4123.

[40]. Y. L. Chiu and A. H. W. Ngan, Time-dependent characteristics of incipient plasticity in nanoindentation of a Ni_3Al single crystal, *Acta Materialia,* Volume 50, Issue 6, 2 April (2002) 1599-1611.

[41]. A. Gouldstone, H. -J. Koh, K. -Y. Zeng, A. E. Giannakopoulos and S. Suresh. Discrete and continuous deformation during nanoindentation of thin films, Acta Materialia, Volume 48, Issue 9, 29 May (2000) 2277-2295.

[42]. J. D. Kiely and J. E. Houston, Nanomechanical properties of Au (111), (001), and (110) surfaces. Physical Review B (Condensed Matter), vol.57, (no.19), (1998) 12588-12594.

[43]. J. Woirgard, C. Tromas, J. C. Girard and V. Audurier, Study of the mechanical properties of ceramic materials by the nanoindentation technique, Journal of the European Ceramic Society, Volume 18, Issue 15, December (1998) 2297-2305.

[44]. M. S. Wu and Y. Yu, Analysis of cracks nucleated by dislocation pile-ups against nonequilibrium grain boundaries, Mechanics of Materials, Volume 32, Issue 9, September (2000) 511-529.

[45]. V. Radmilovic, D, Gao, U. Dahmen, C. R. Stoldt, C. Carraro, and R. Maboudian, Nucleation and growth of 3C-SiC film on Si (100) substrate, Submitted to Applied Physics Letters, (2003).

[46]. Di Gao, Muthu B. J. Wijesundara, Roger T. Howe and Roya Maboudian, Characterization of residual strain in SiC films deposited using 1,3-dislabutane for MEMS application, submitted (2003).

[47]. N. R. Moody, D. Medlin, D. Boehme and D. P. Norwood, Film thickness effects on the fracture of tantalum nitride on aluminum nitride thin film systems, Engineering Fracture Mechanics, Volume 61, Issue 1, August (1998) 107-118.

[48]. K. Sriram, R. Narasimhan and S. K. Biswas, A numerical fracture analysis of indentation into thin hard films on soft substrates, Engineering Fracture Mechanics, In Press, Corrected Proof, Available online 13 September (2002).

[49]. D. B. Marshall and A. G. Evans, Measurement of adherence of residually stressed thin films by indentation. I. Mechanics of interface delamination, *J. Appl. Phys.* **56** (1984) 2632–2638.

[50]. S. Nogami, A. Hasegawa, and L. L. Snead, Indentation fracture toughness of neutron irradiated silicion carbide, Journal of Nuclear Materials 307-311 (2002) 1163-1167.

[51]. G. Yu, H. Ishikawa, T. Egawa, T. Soga, J. Watanabe, T. Jimbo and M. Umeno, Mechanical properties of the GaN thin films deposited on sapphire substrate, Journal of Crystal Growth, Volumes 189-190, 15 June (1998) 701-705.

[52]. R. Andersson, G. Toth, L. Gan and M. V. Swain, Indentation response and cracking of sub-micron silica films on a polymeric substrate, Engineering Fracture Mechanics, Volume 61, Issue 1, August (1998) 93-105.

[53]. C. L. Woodcock and D. F. Bahr, Plastic zone evolution around small scale indentations, Scripta Materialia, Volume 43, Issue 9, 16 October (2000) 783-788.

[54]. Natalia I. Tymiak, Antanas Daugela, Thomas J. Wyrobek, and Oden L.Warren. Highly localized Acoustic Emission monitoring of nanoscale indentation contacts, Submitted 2003.

[55]. Yasuhide Shindo, Naoki Niwa and Ryuichi Togawa, Multiple scattering of antiplane shear waves in a fiber-reinforced composite medium with interfacial layers,

International Journal of Solids and Structures, Volume 35, Issues 7-8, March (1998) 733-745.

List of Figures

List of Tables

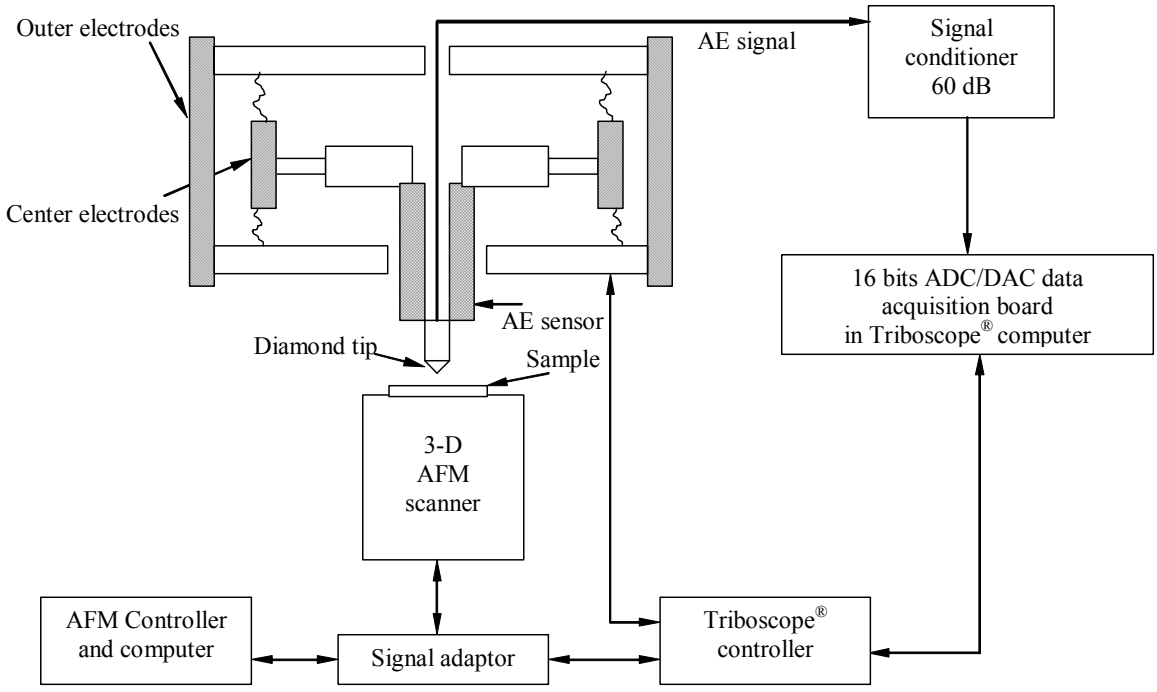

Figure 1. Diagram of the AE nanoindentation system

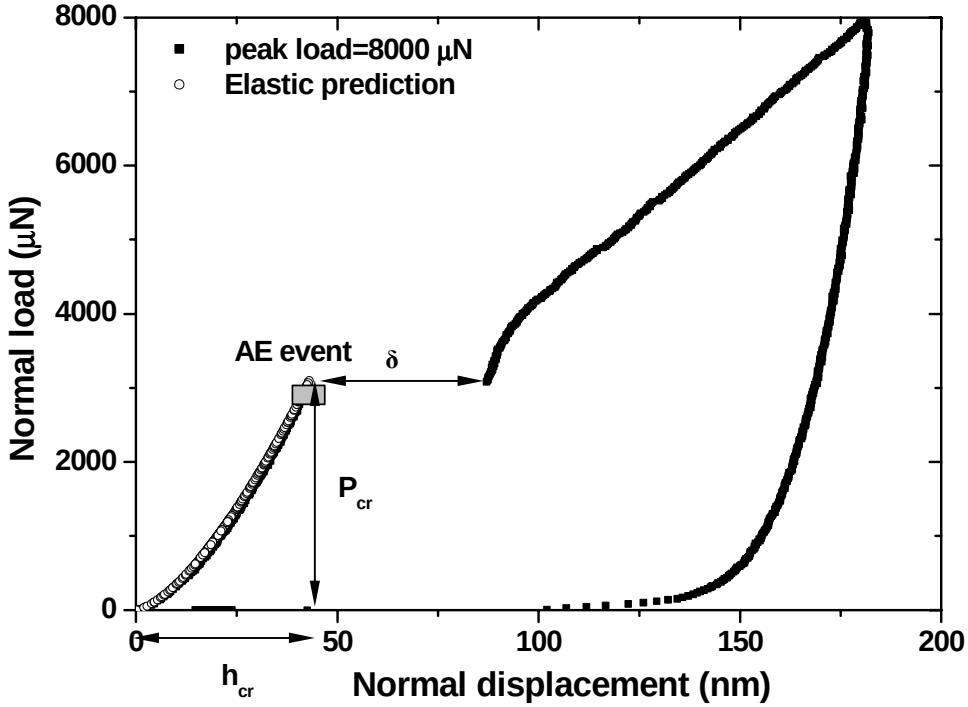

(a)

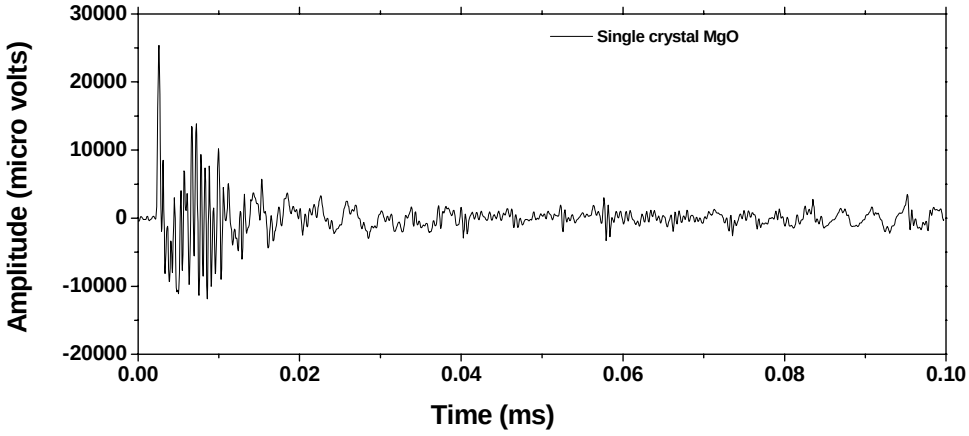

(b)

Figure 2. (a) A load-unload curve of an indentation into single crystal MgO using a cubic corner tip with nominal radius of curvature equal to 685 nm, and the elastic prediction by equation 1. (b) corresponding AE signal captured.

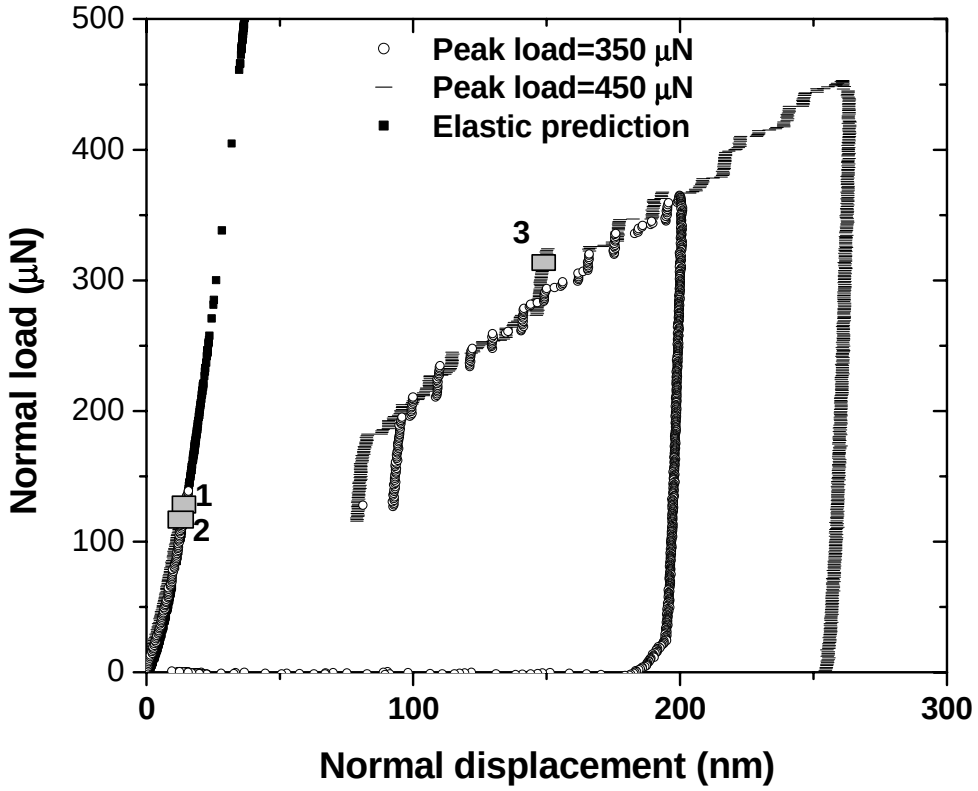
Peak load=350 μN
Peak load=450 μN
Elastic prediction
Normal load (μN)
Normal displacement (nm)
1
2
3
0
100
200
300
400
500

(a)

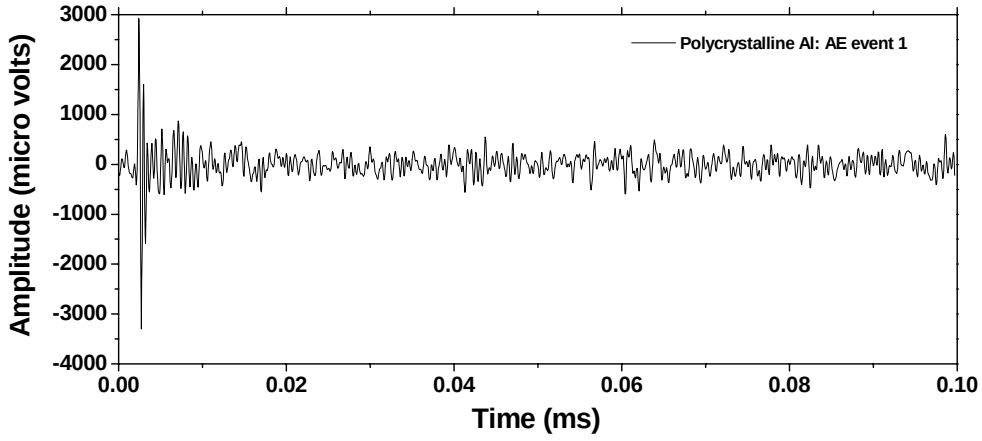
Polycrystalline Al: AE event 1
Amplitude (micro volts)
Time (ms)
3000
2000
1000
0
-1000
-2000
-3000
-4000
0.00
0.02
0.04
0.06
0.08
0.10

(b)

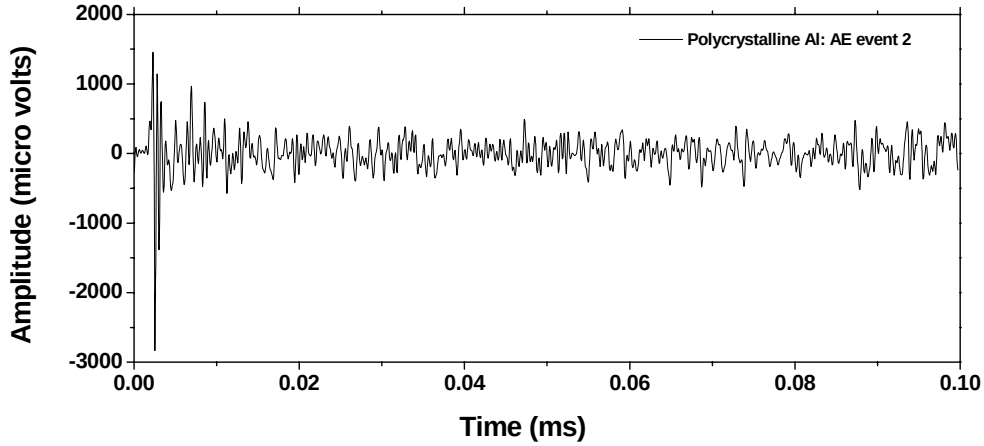

(c)

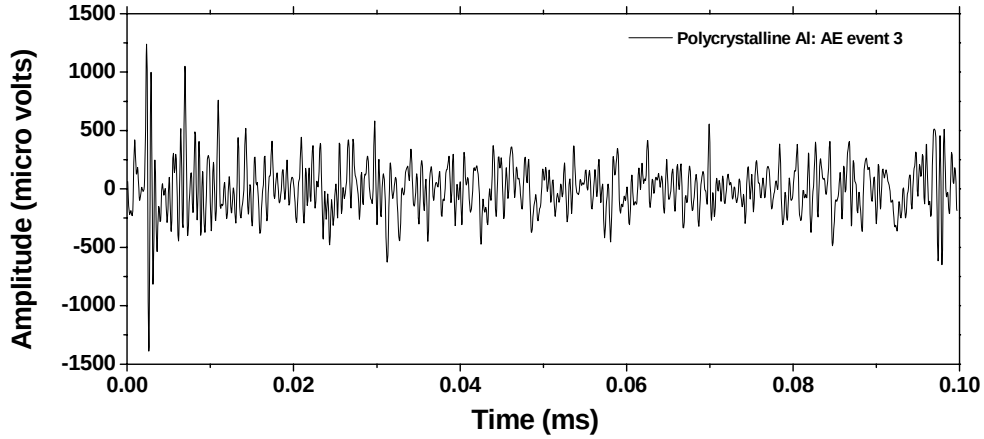

(d)

Figure 3. (a) Load-unload curves of indentations into an electropolished polycrystalline Al foil using a cubic corner tip with nominal radius of curvature equal to 685 nm and (b), (c), and (d) corresponding AE signal captured.

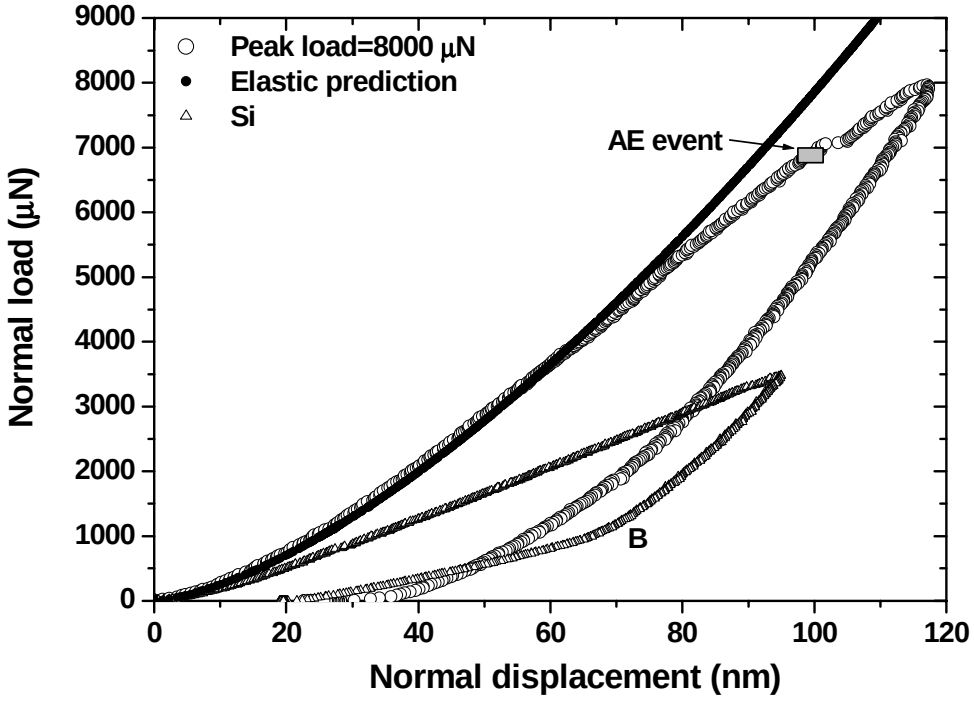

(a)

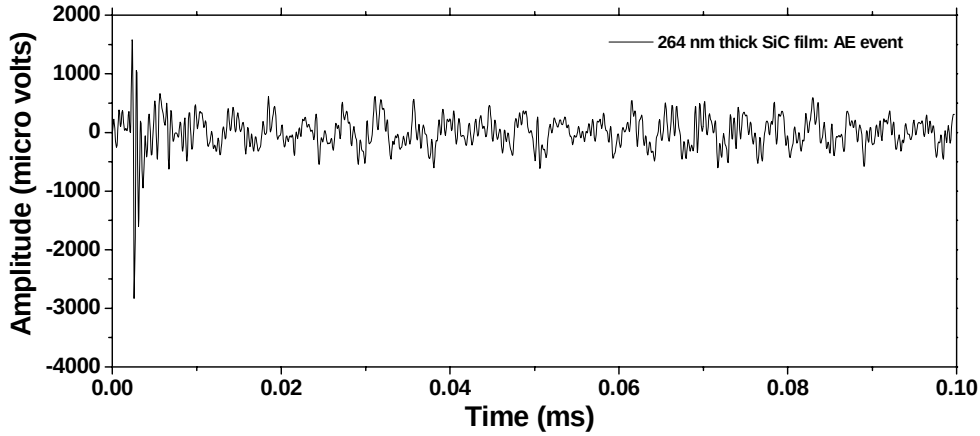

(b)

Figure 4. (a) A load-unload curve of an indentation into a 264 nm thick polycrystalline SiC film and substrate, respectively, using a 685 nm radius tip and the elastic prediction by equation 1. (b) corresponding AE signal captured.

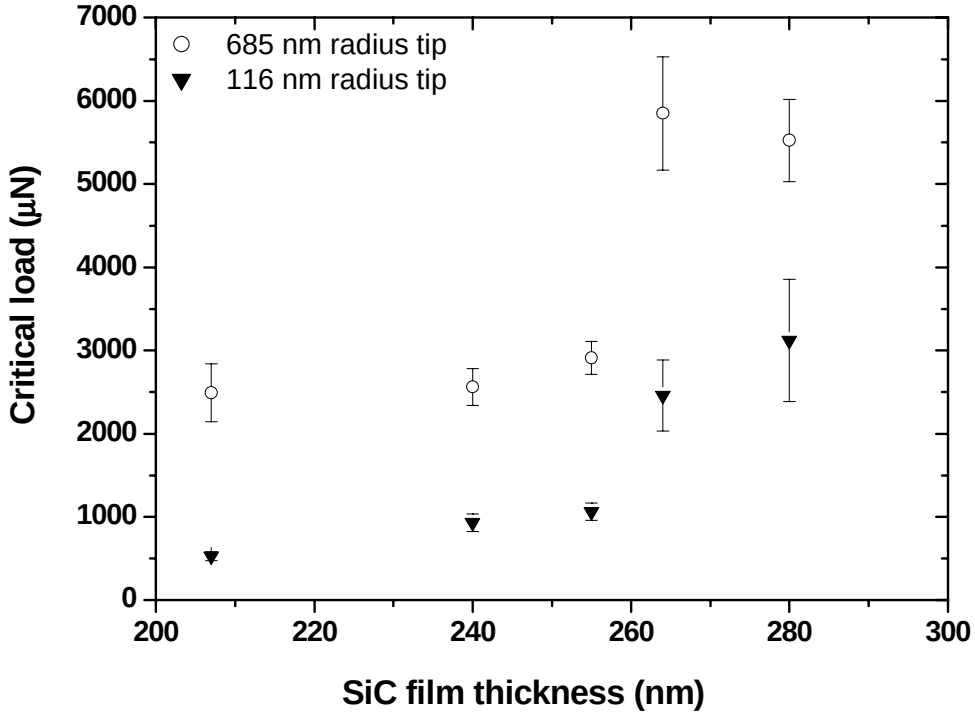

Figure 5. Thickness dependence of critical loads for polycrystalline SiC films. Error bar shows the standard deviation from more than 30 indentation data.

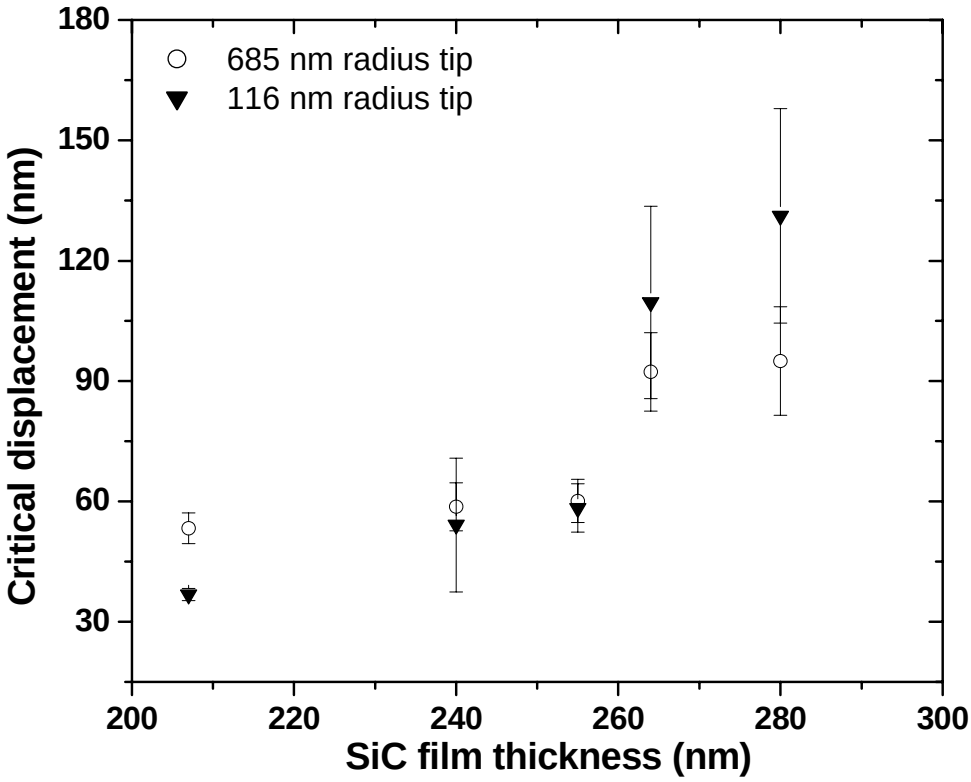

Figure 6. Thickness dependence of critical displacements for polycrystalline SiC films. Error bar shows the standard deviation from more than 30 indentation data.

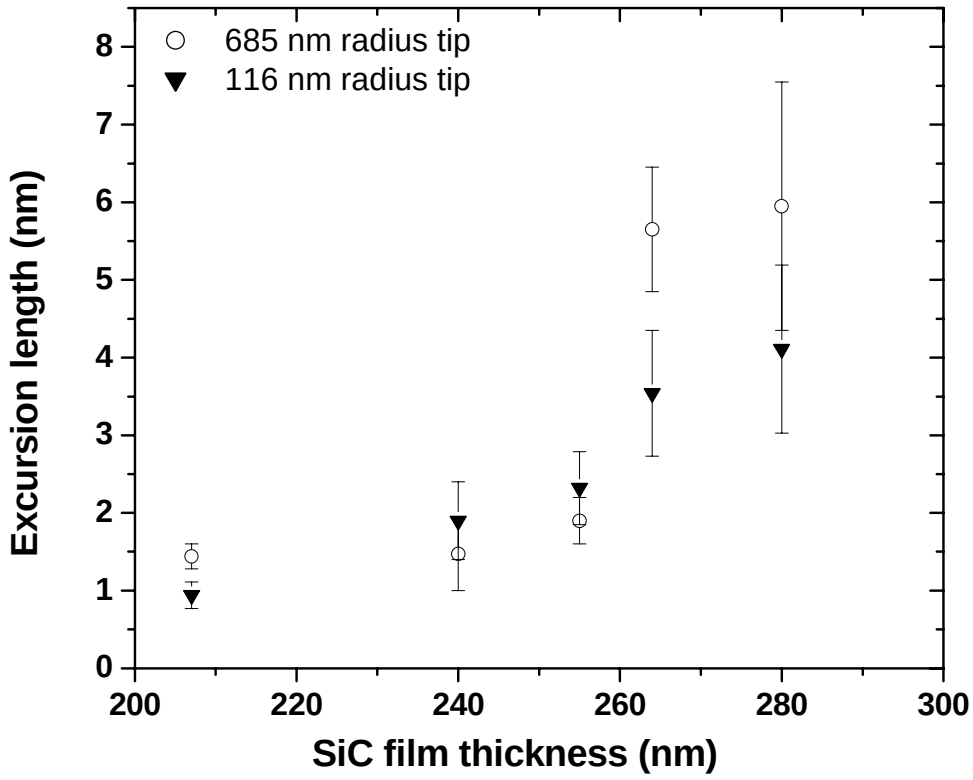

Figure 7. Excursion lengths as a function of SiC film thickness. Error bar shows the standard deviation from more than 30 indentation data.

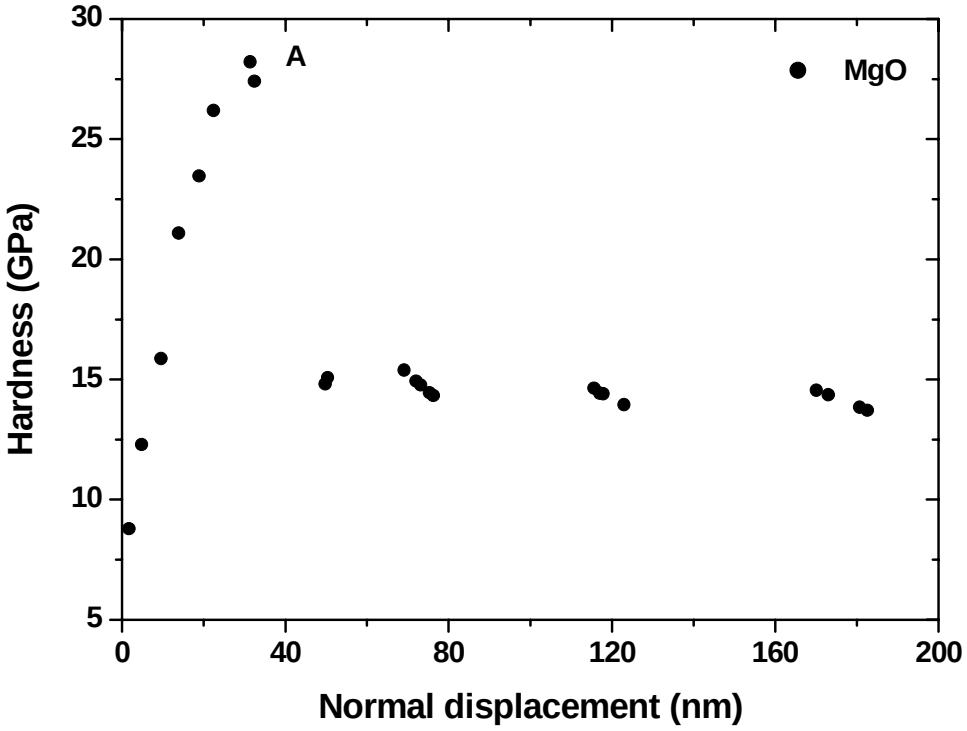

Figure 8. Hardness of single crystal MgO as a function of normal displacement.

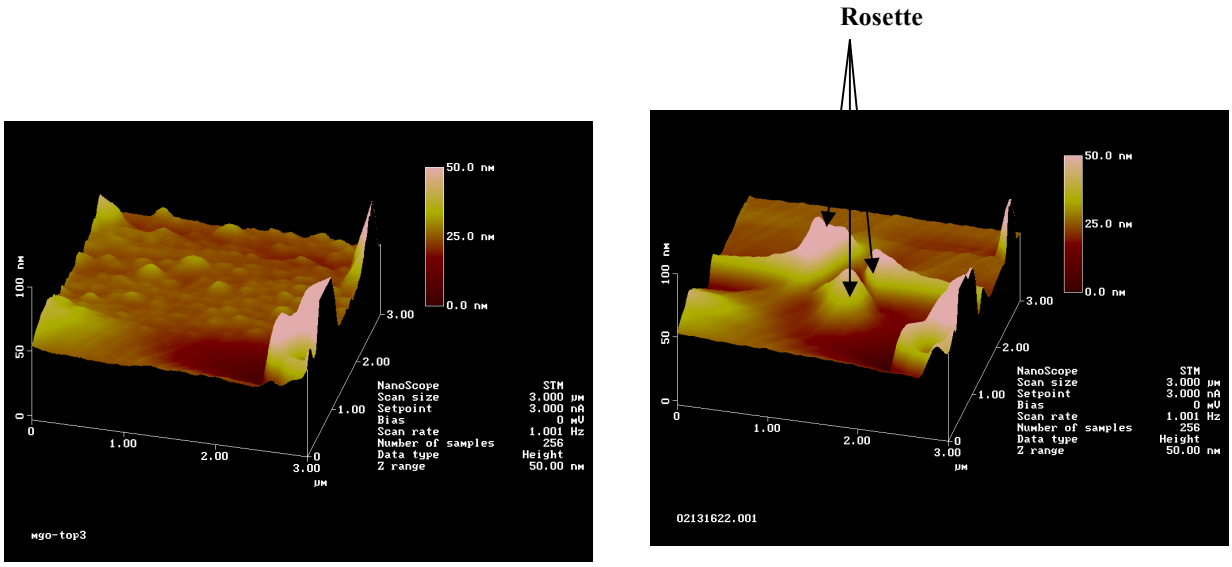

Figure 9. SPM images of single crystal MgO. (a) surface view before nanoindentation, (b) surface view after nanoindentation with maximum load of 5000 μN.

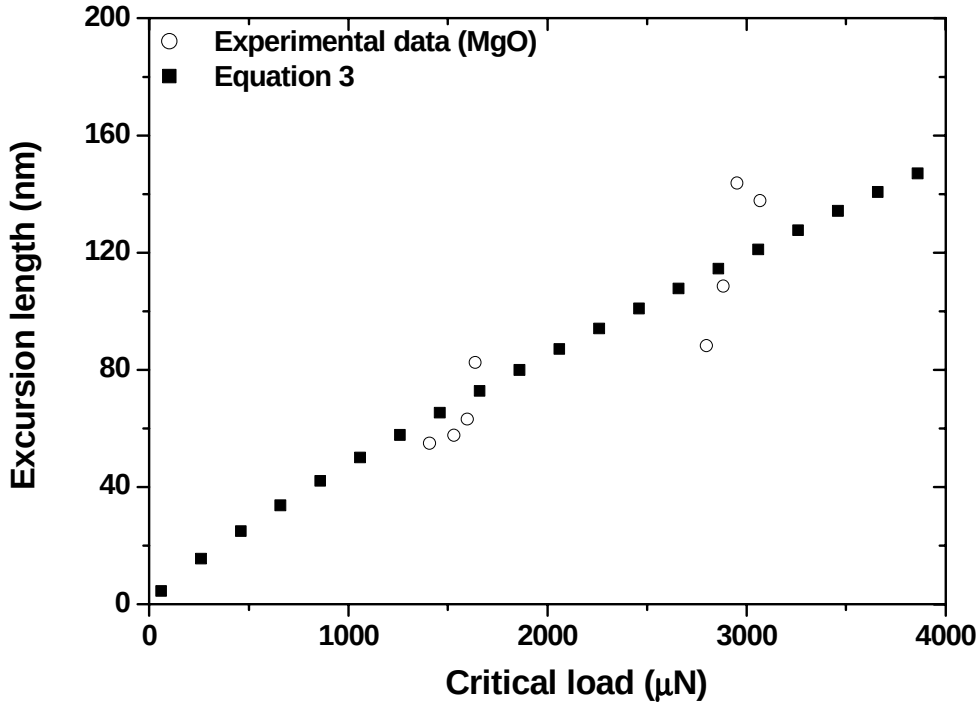

Figure10. Excursion length as a function of critical load. The experimentally measured values for single crystal MgO are compared to the theoretical values calculated by equation (2).

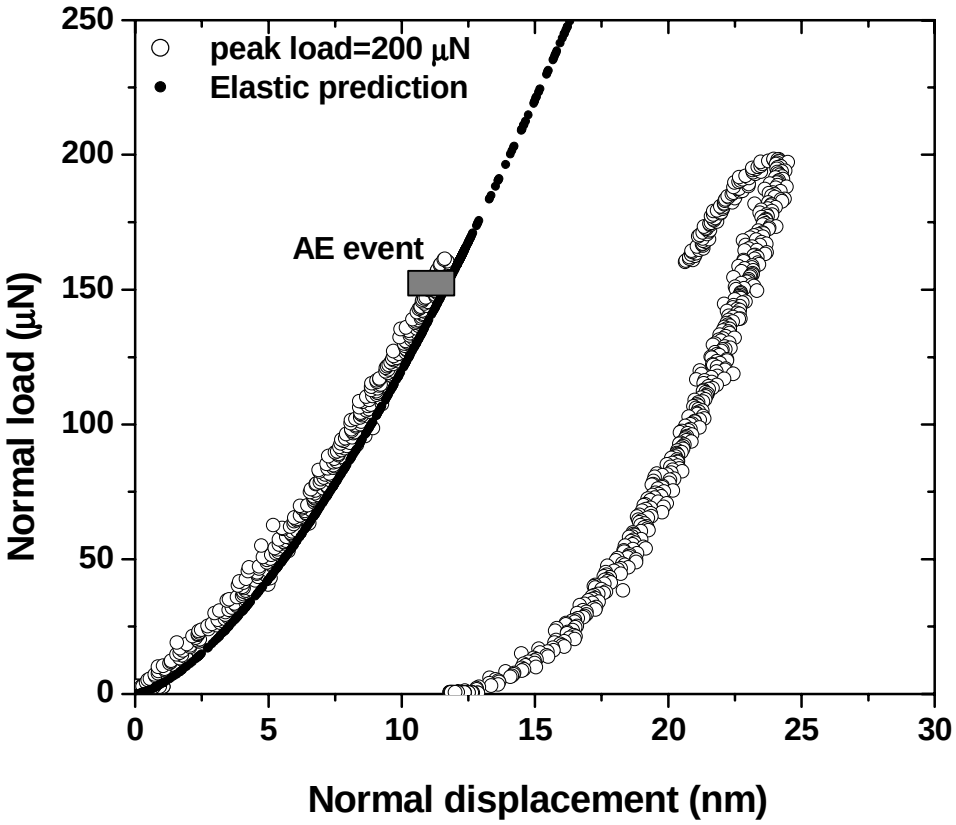

(a)

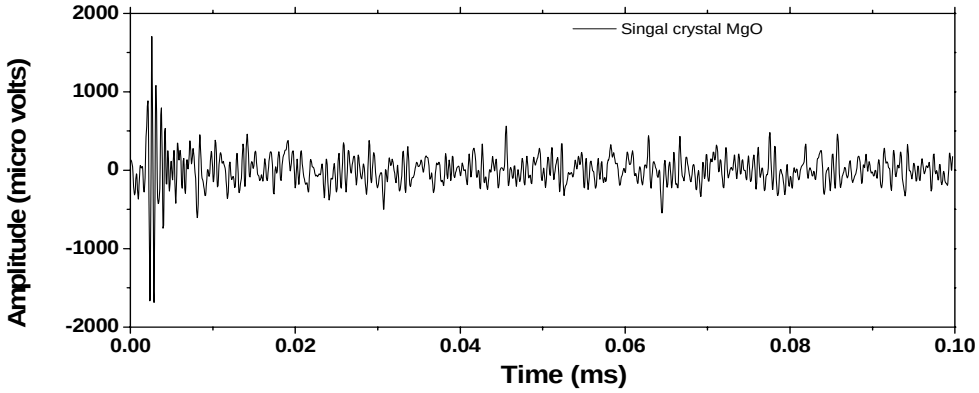

(b)

Figure 11. (a) A load-unload curve of an indentation into single MgO crystalline using a 116 nm radius tip and the elastic prediction by equation 1. (b) corresponding AE signal captured.

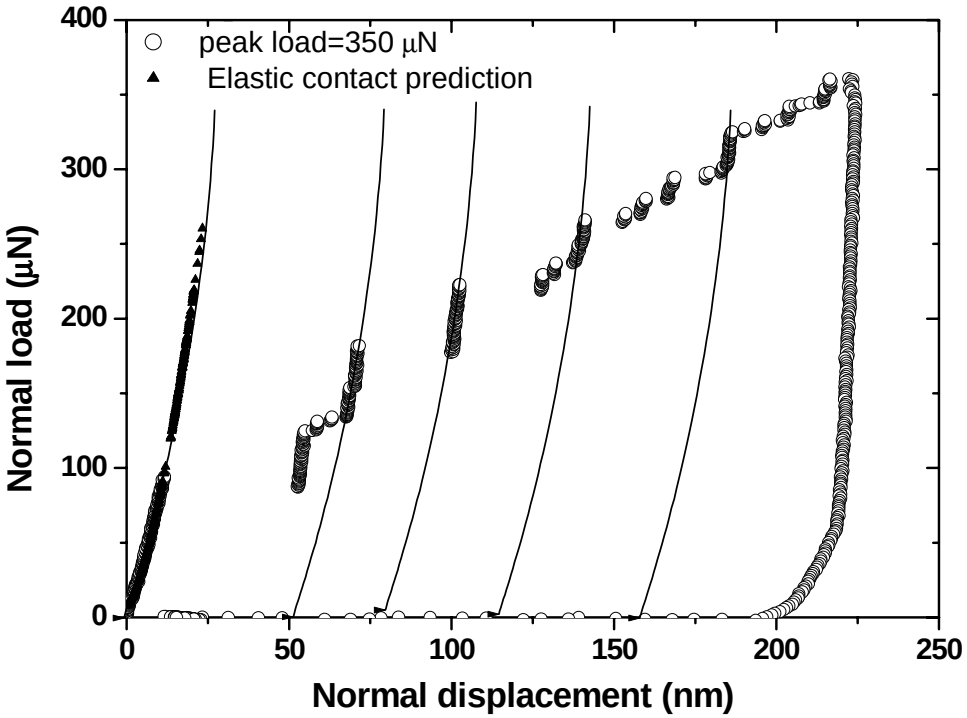

Figure 12. A load-unload curve of an indentation into polycrystalline Al using a 685 nm radius tip and the elastic prediction by equation 1.

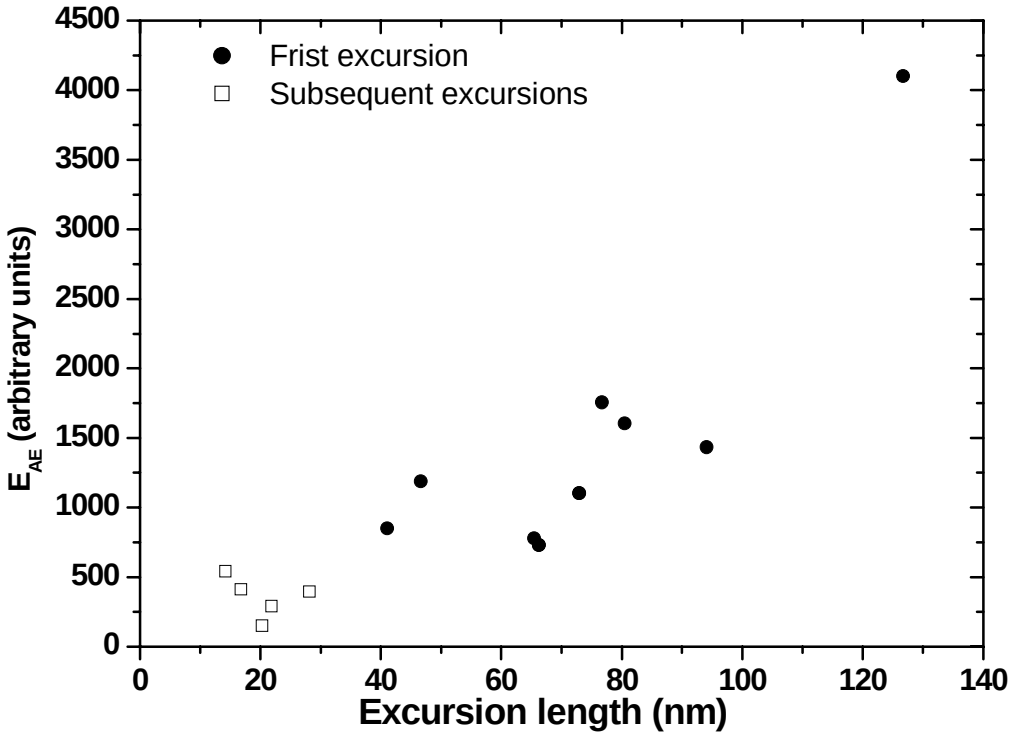

Figure 13. AE energy of first and subsequent 'pop-ins' as a function of excursion lengths for a polycrystalline Al.

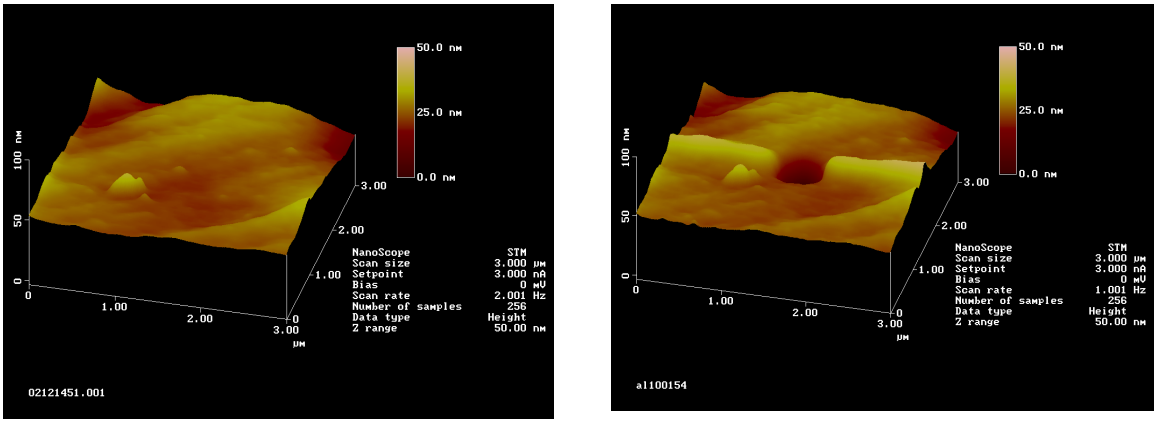

Figure 14. SPM images of polycrystalline Al (a) surface view before nanoindentation, (b) surface view after nanoindentation with maximum load of 150 μN.

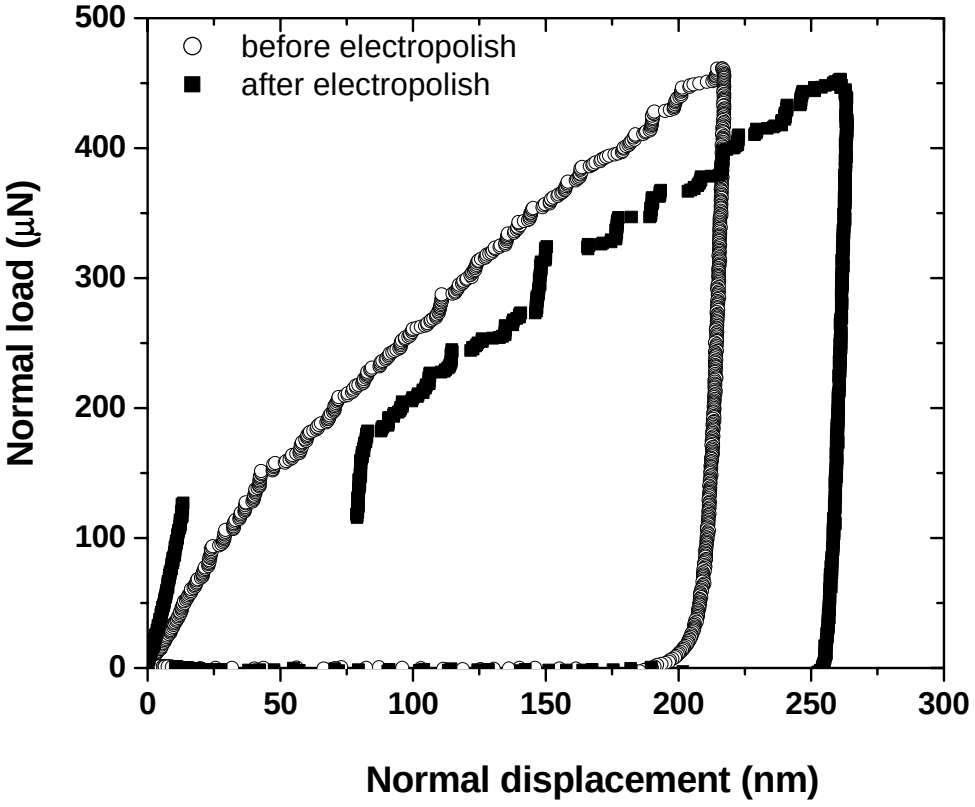

Figure 15. Load-unload curves before and after electropolishing polycrystalline Al with a 685 nm radius tip.

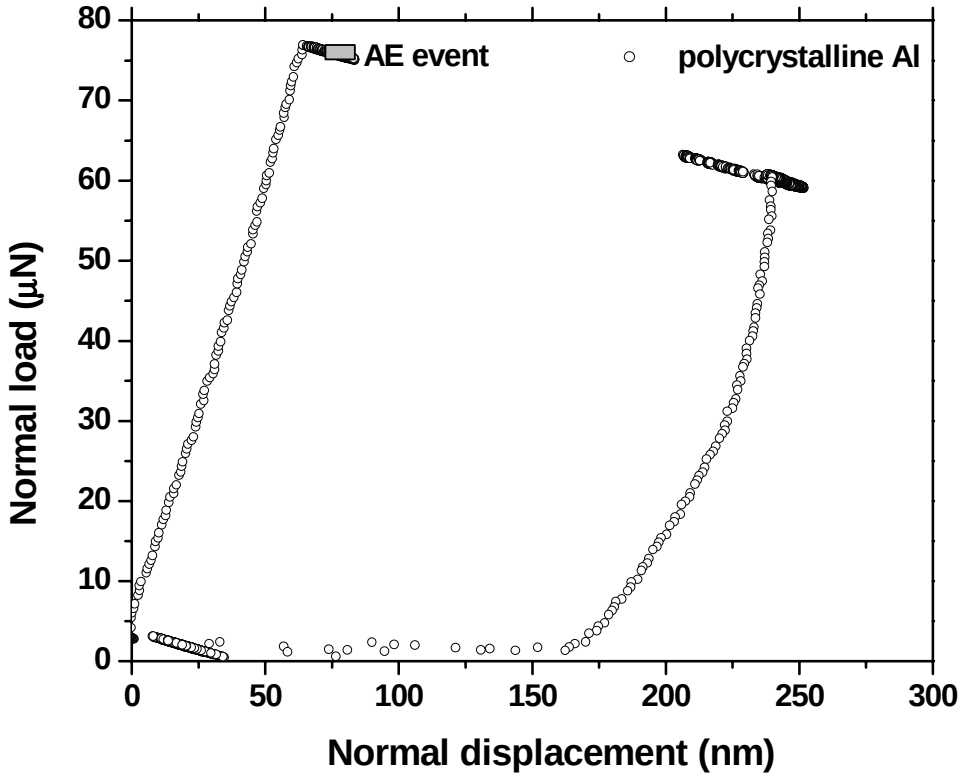

(a)

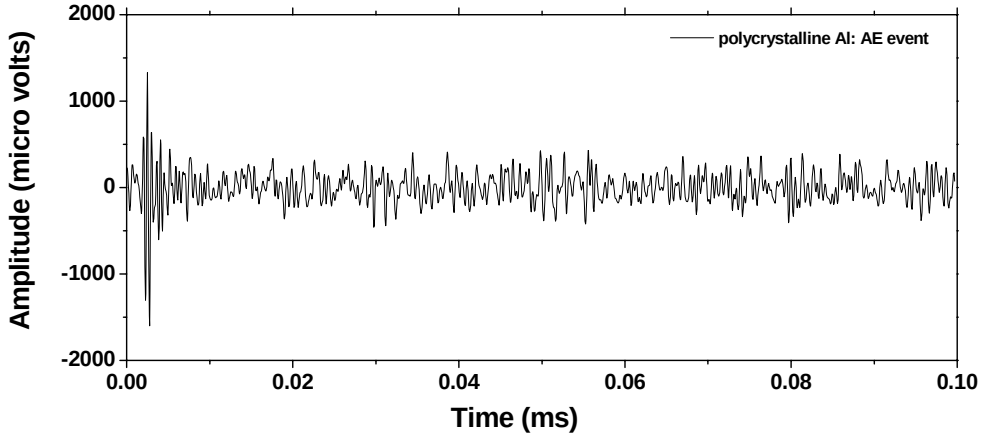

(b)

Figure 16. (a) A load-unload curve for polycrystalline Al with a 685 radius tip, with a time-dependent 'pop-in', (b) corresponding AE signal.

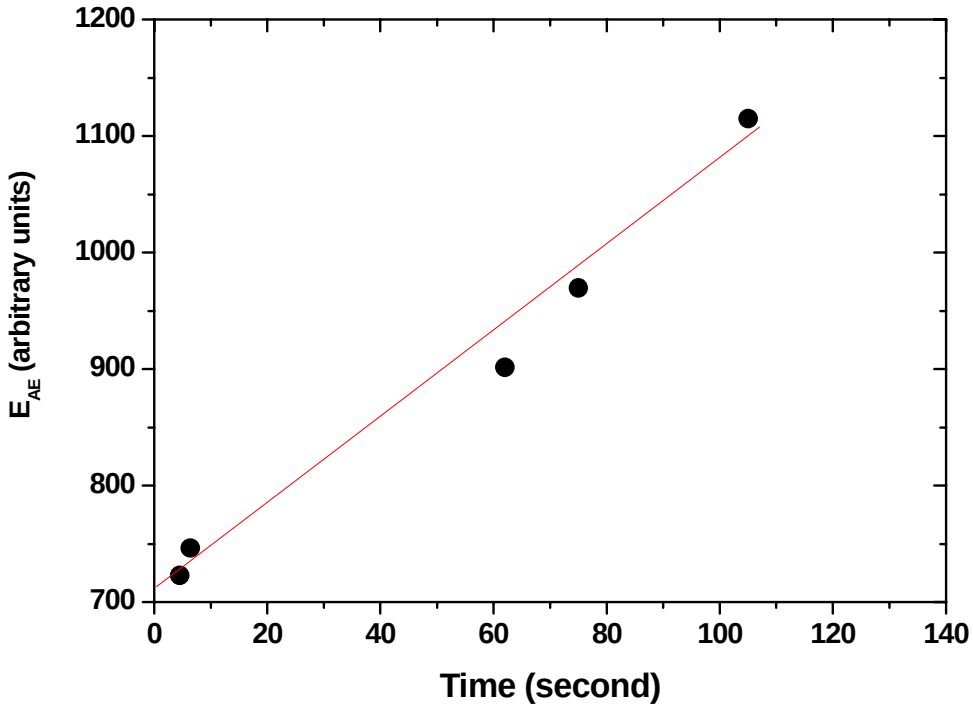

Figure 17. AE energy as a function of waiting time for 'pop-in' to occur during load holding on polycrystalline Al with a 685 nm radius tip.

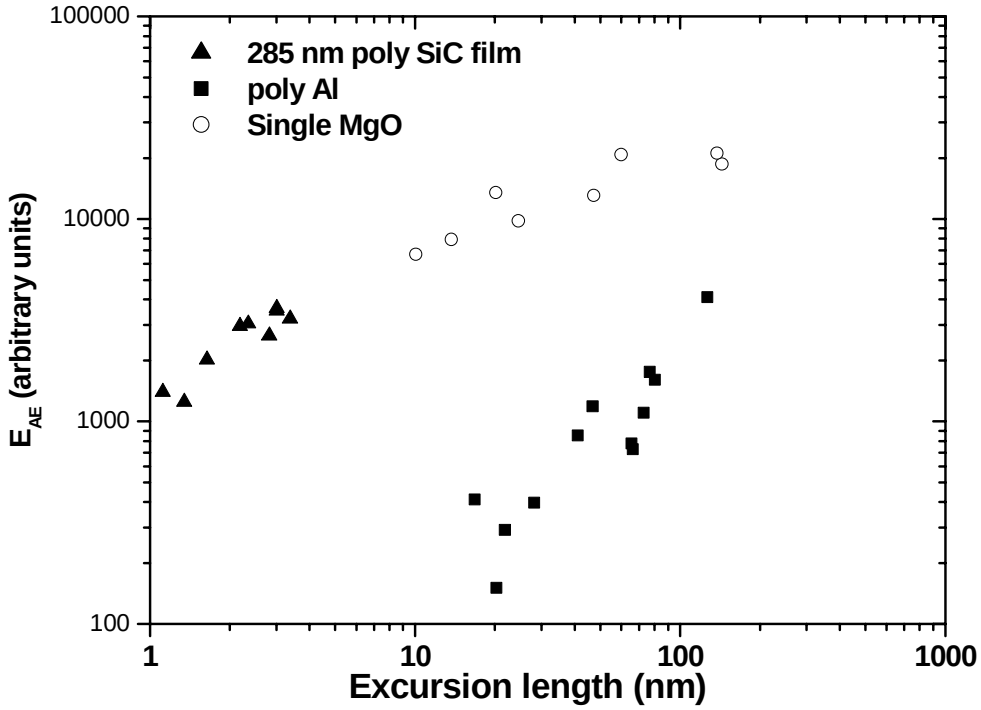

Figure 18. AE energy comparison for polycrystalline SiC films, polycrystalline Al and single MgO vs. excursion length with a 685 nm radius tip.

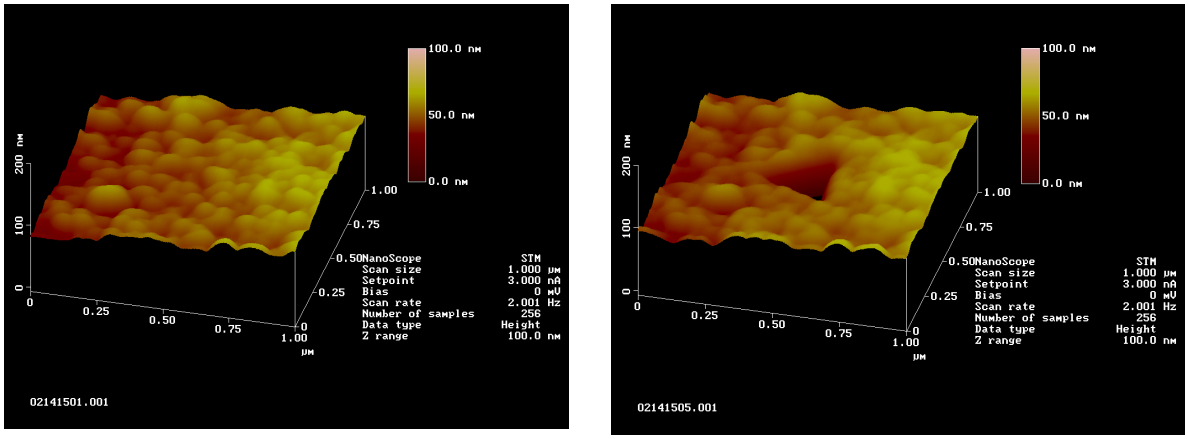

Figure 19. SPM images of polycrystalline SiC film. (a) surface view before nanoindentation, (b) surface view after nanoindentation with maximum load of 3000 µN.

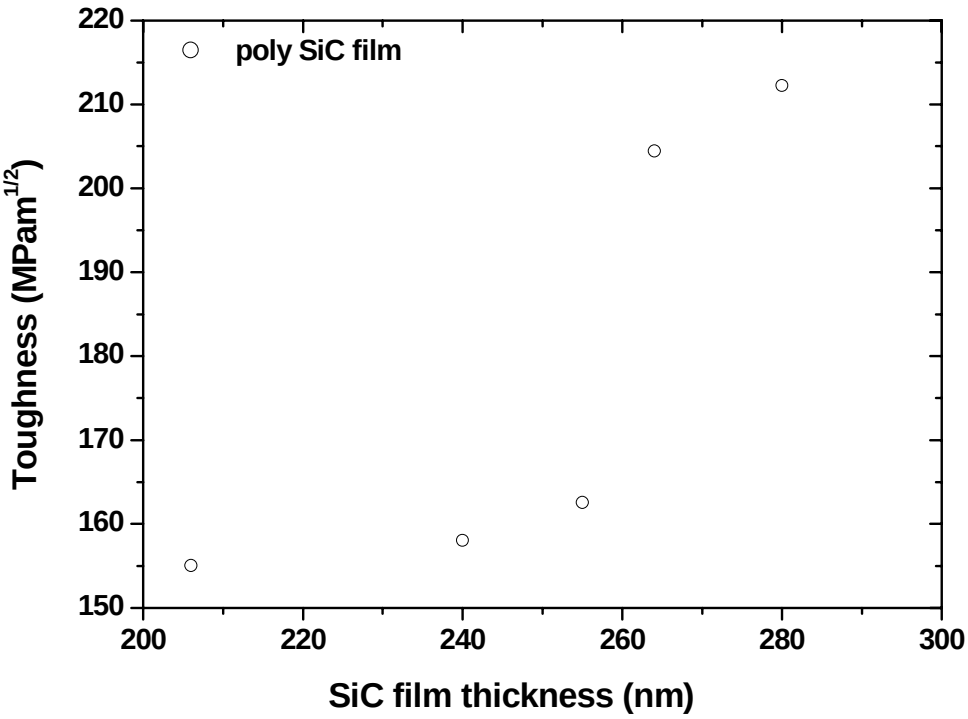

Figure 20 Toughness as a function of SiC film thickness.

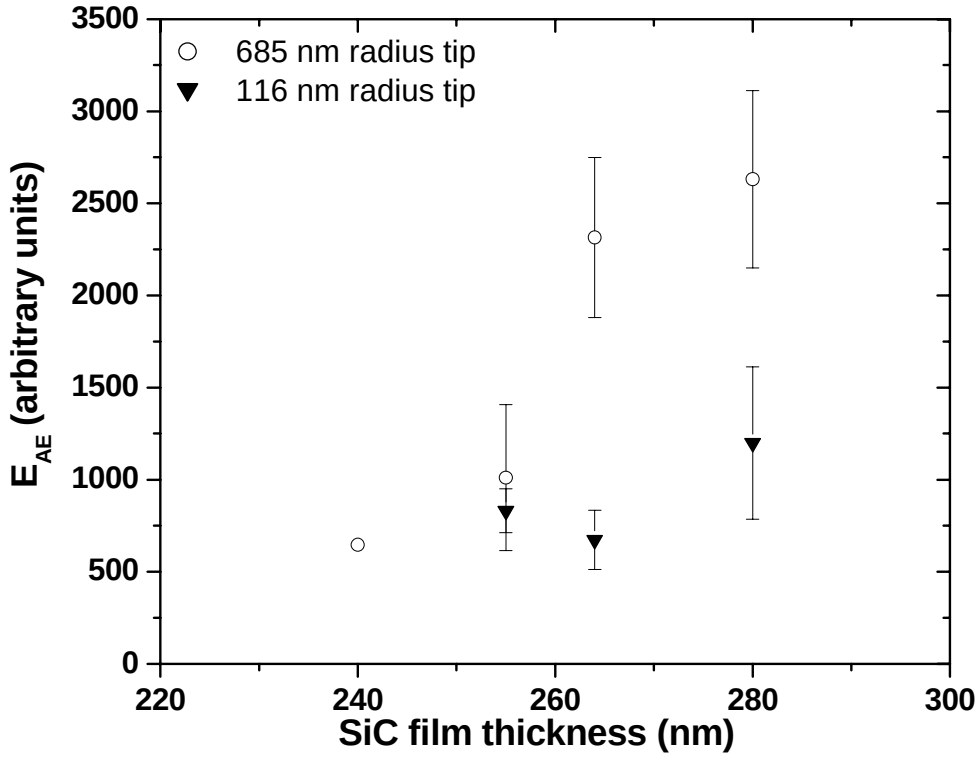

Figure 21 AE energy as a function of SiC films thickness. Error bar shows the standard deviation from more than 30 indentation data.

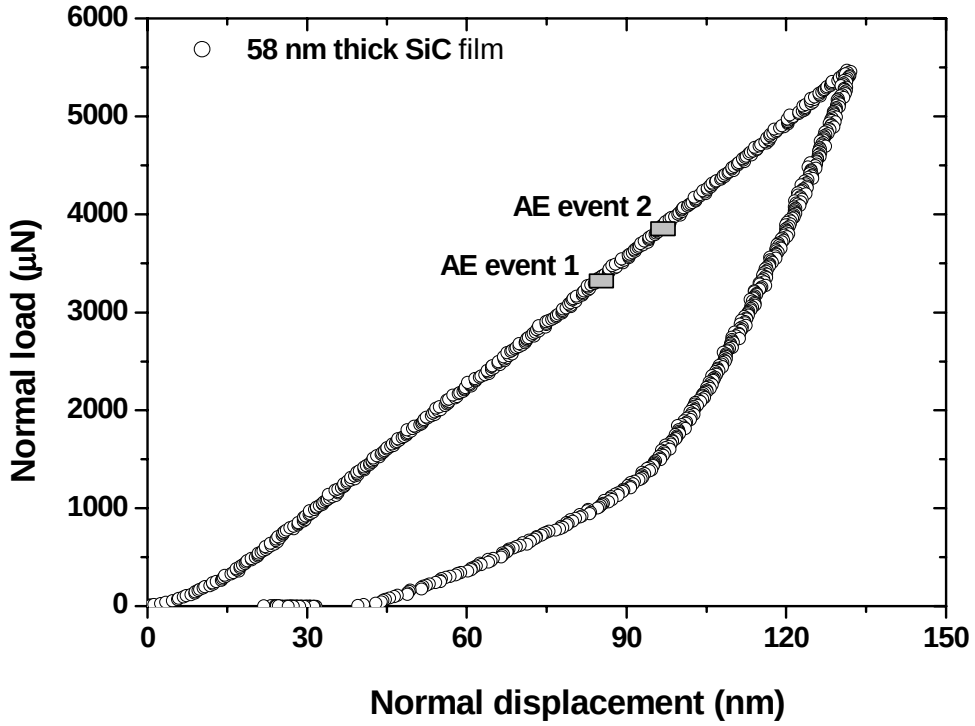
58 nm thick SiC film
AE event 2
AE event 1
Normal load (μN)
Normal displacement (nm)
6000
5000
4000
3000
2000
1000
0
0
30
60
90
120
150

(a)

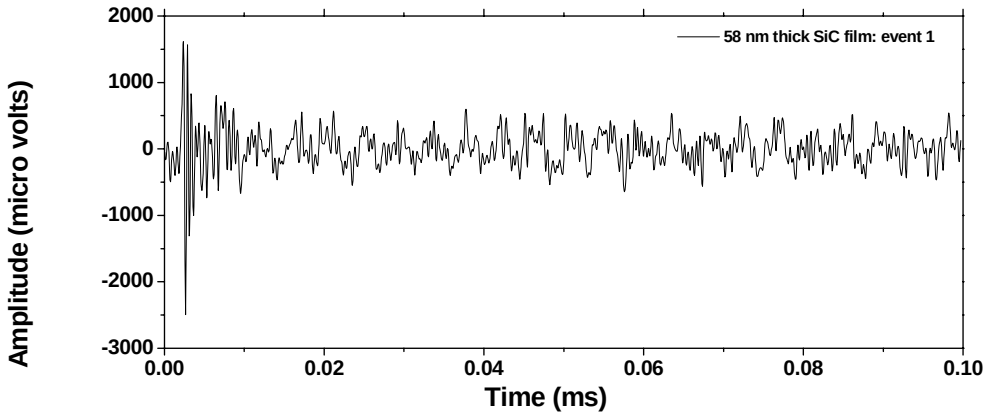
58 nm thick SiC film: event 1
Amplitude (micro volts)
Time (ms)
2000
1000
0
-1000
-2000
-3000
0.00
0.02
0.04
0.06
0.08
0.10

(b)

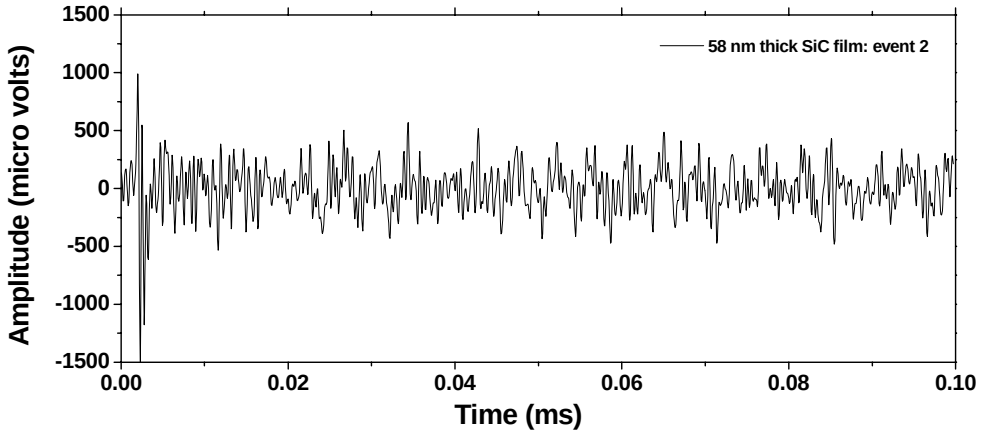

(c)

Figure 22 (a) A load-unload curve of an indentation into a 58 nm thick polycrystalline SiC film using a 685 nm radius tip, (b) and (c) corresponding AE signal captured.

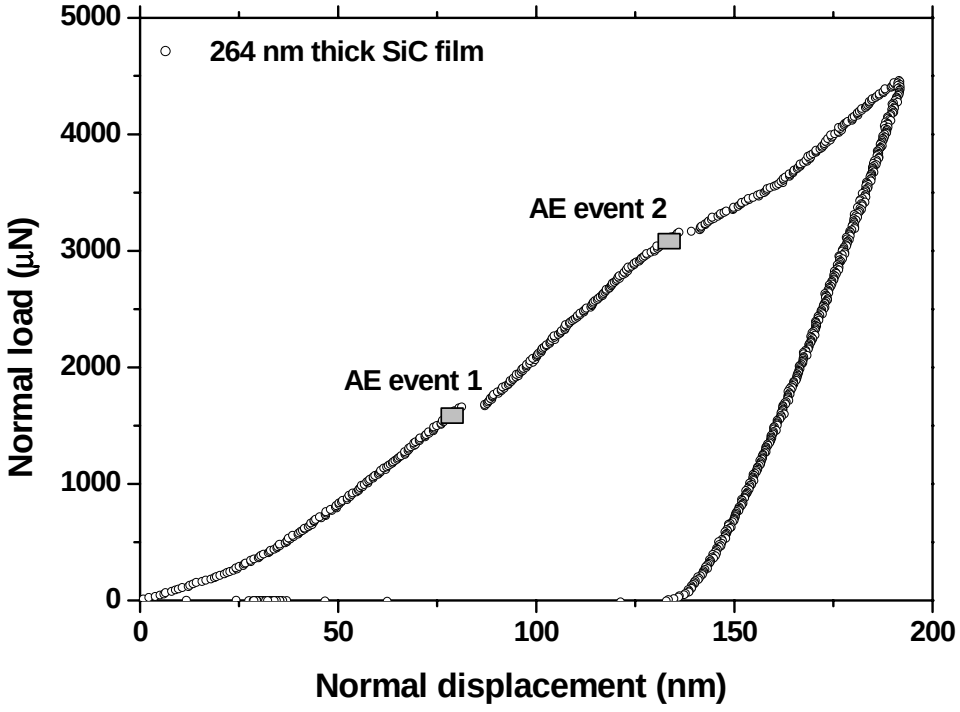
264 nm thick SiC film
AE event 2
AE event 1
Normal load (μN)
Normal displacement (nm)
5000
4000
3000
2000
1000
0
0
50
100
150
200

(a)

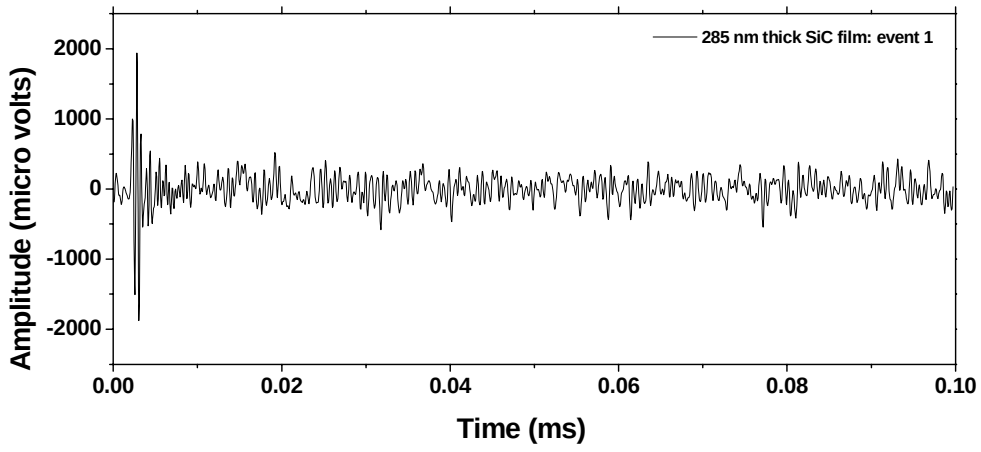
285 nm thick SiC film: event 1
Amplitude (micro volts)
Time (ms)
2000
1000
0
-1000
-2000
0.00
0.02
0.04
0.06
0.08
0.10

(b)

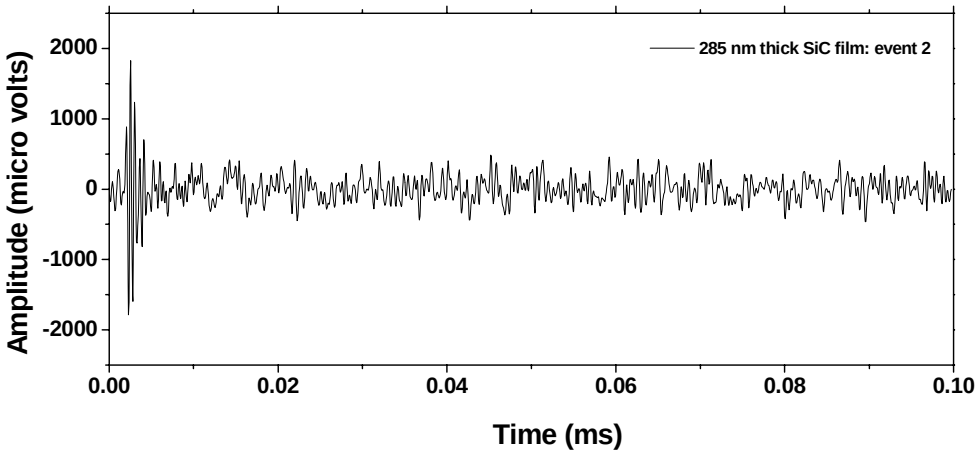

(c)

Figure 23 (a) A load-unload curve of an indentation into a 264 nm thick polycrystalline SiC film using a 116 nm radius tip, (b) and (c) corresponding AE signal captured.

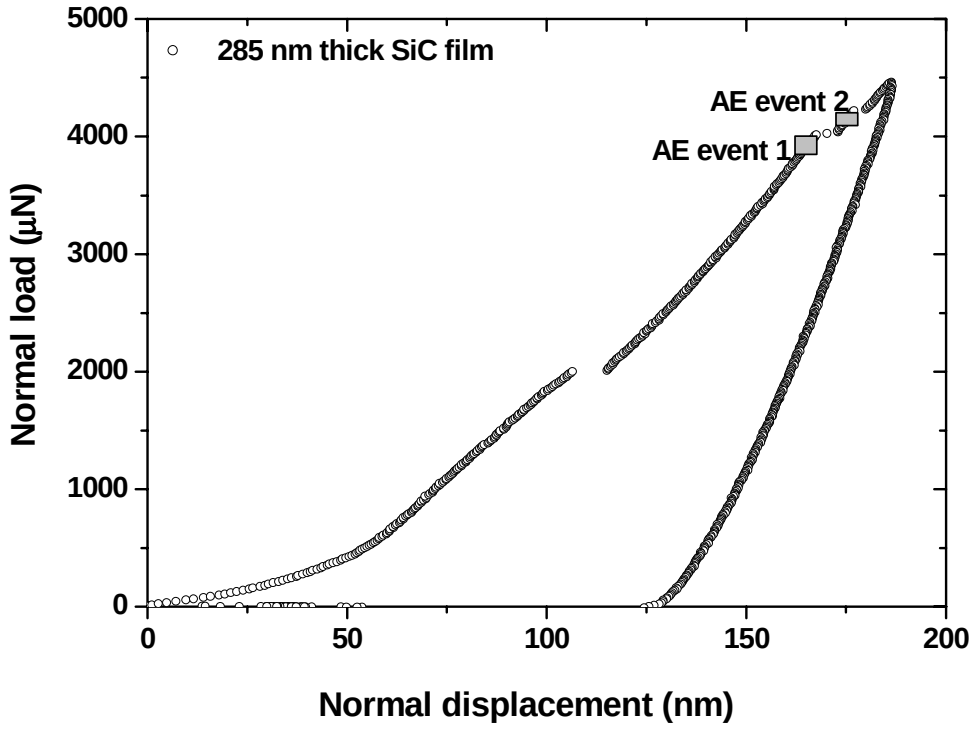
285 nm thick SiC film
AE event 2
AE event 1
Normal load (μN)
Normal displacement (nm)
5000
4000
3000
2000
1000
0
0
50
100
150
200

(a)

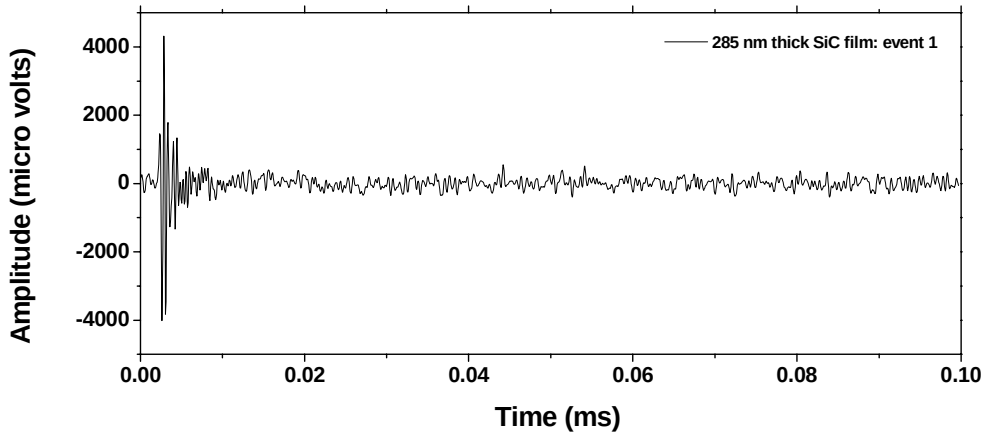
285 nm thick SiC film: event 1
Amplitude (micro volts)
Time (ms)
4000
2000
0
-2000
-4000
0.00
0.02
0.04
0.06
0.08
0.10

(b)

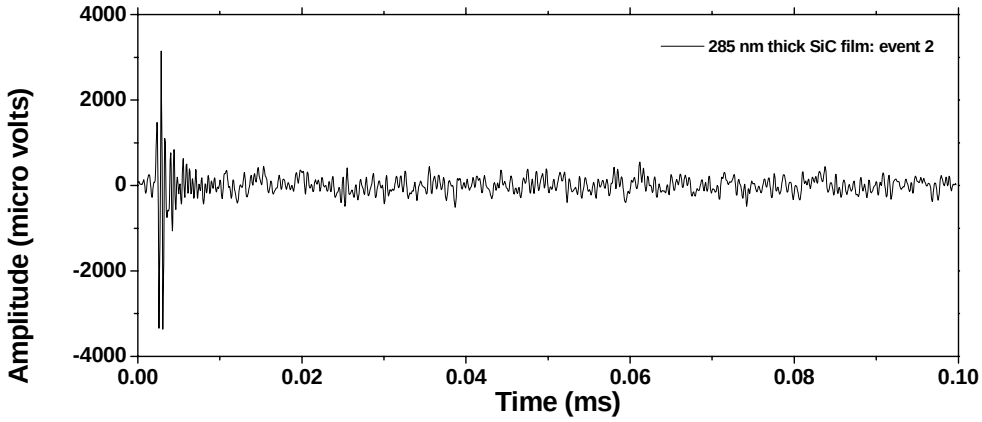

(c)

Figure 24 (a) A load-unload curve of an indentation into a 285 nm thick polycrystalline SiC film using a 116 nm radius tip, (b) and (c) corresponding AE signal captured.

Table 1 Mechanical properties of the SiC films with different thickness.

Thickness (nm)	Hardness (GPa)	Reduced Young.s modulus (GPa) <sd>
58	34.0	186.8 <15.18>
150	38.7	193.5 <16.4>
206.7	50.52	233.58 <14.6>
240.4	48.43	249.6<19.1>
255	45.8	274.8 <17.3>
264	45.45	284.1 <12.1>
285	42.62	281.3 <16.1>
1355	31.45	341.8 <13.8>

Table 2. AE characteristics of single crystal MgO

Tip radius (nm)	685 <Sd>	116 <Sd>
P_{cr} (μN)	1621.3 <114.1>	140.0 <28.4>
δ (nm)	17.1 <3.5>	7.14 <2.7>
E_{AE} (arbitrary units)	13924 <5685>	1782 <347>

Table 3. Comparison of theoretical shear strength and maximum shear stress.

Material	Maximum shear stress (GP)	Theoretical Shear strength (GPa)
Single crystal MgO	21.65	23.55[a]
Poly Al foil	4.07	4.2 [40]
Poly 3c-SiC	10.22	29.95[b]

[a]: calculated by using G=148 GPa[35]
[b]: calculated by using G=188.1 GPa [55]

Table 4. Statistics of the indentations with AE sensor

Tip radius (nm)	Thickness (nm)	# of indentations with no excursions	# of indentations with excursions but no AE signals captured	# of indentations with excursions and AE signals captured
685	**207**	**17**	**2**	**0**
	240	**16**	**15**	**1**
	255	**5**	**18**	**5**
	264	**8**	**4**	**16**
	285	**0**	**0**	**56**
116	**207**	**27**	**5**	**0**
	240	**21**	**12**	**0**
	255	**15**	**18**	**3**
	264	**13**	**23**	**5**
	285	**0**	**24**	**13**